Published in final edited form as:
Dev Cell. 2023 December 04; 58(23): 2700–2717.e12. doi:10.1016/j.devcel.2023.10.010.

A SOX9-B7x axis safeguards dedifferentiated tumor cells from immune surveillance to drive breast cancer progression

Yu Liu[1,2], **Peter John**[3], **Kenta Nishitani**[1,2], **Jihong Cui**[1,2], **Christopher D. Nishimura**[3], **John R. Christin**[1,2], **Nicole Couturier**[3], **Xiaoxin Ren**[3], **Yao Wei**[3], **Marc C. Pulanco**[3], **Phillip M. Galbo Jr.**[3,4], **Xusheng Zhang**[4], **Wenyan Fu**[1,2], **Wei Cui**[3], **Boris A. Bartholdy**[2], **Deyou Zheng**[4,5], **Gregoire Lauvau**[3], **Susan A. Fineberg**[6], **Maja H. Oktay**[6,7,8,9,10], **Xingxing Zang**[3,11,12,*], **Wenjun Guo**[1,2,7,*]

[1]Ruth L. and David S. Gottesman Institute for Stem Cell and Regenerative Medicine Research, Albert Einstein College of Medicine, Bronx, NY 10461, USA

[2]Department of Cell Biology, Albert Einstein College of Medicine, Bronx, NY 10461, USA

[3]Department of Microbiology and Immunology, Albert Einstein College of Medicine, Bronx, NY 10461, USA

[4]Department of Genetics, Albert Einstein College of Medicine, Bronx, NY 10461, USA

[5]Departments of Neurology and Neuroscience, Albert Einstein College of Medicine, Bronx, NY 10461, USA

[6]Department of Pathology, Albert Einstein College of Medicine/Montefiore Medical Center, Bronx, NY 10467, USA

[7]Montefiore Einstein Comprehensive Cancer Center, Albert Einstein College of Medicine, Bronx, NY 10461, USA

---

[*]Correspondence: wenjun.guo@einsteinmed.edu; xingxing.zang@einsteinmed.edu.
Lead Contact: Wenjun Guo (wenjun.guo@einsteinmed.edu)

AUTHOR CONTRIBUTIONS

Y.L. designed and performed the experiments, acquired and analyzed data; P.J. performed immune checkpoint profiling for SGC tumor and immune cell profiling for anti-B7x treatment; M.O. identified the immune infiltration phenotype; J.R.C. contributed to immune cell and checkpoint analyses; C.D.N. performed T-cell coculture and cytotoxicity assays; N.C developed and assisted the Cytek Aurora analysis under the supervision of G.L.; P.J. and X.R. performed coculture proliferation assay; K.N. performed ELISA assay and immune cell profiling; P.M.G. and B.B. analyzed epigenomics data with supervision of D.Z.; Y.W., M.C.P., and W.C. generated B7x monoclonal antibodies; J.C. characterized the SGC tumor model and in vivo treatment experiments; W.F. contributed to antibody treatment experiments; Xu.Z. performed scRNA-seq and TCGA BRCA gene set enrichment analysis; S.A.F contributed to human DCIS analyses; Y.L., X.Z., and W.G. wrote the manuscript with inputs from all other authors; X.Z. and W.G. supervised the study.

DECLARATION OF INTERESTS

The authors declare no competing interests.

INCLUSION AND DIVERSITY

One or more of the authors of this paper self-identifies as an underrepresented ethnic minority in their field of research or within their geographical location. One or more of the authors of this paper self-identifies as a gender minority in their field of research. One or more of the authors of this paper self-identifies as a member of the LGBTQIA+ community. One or more of the authors of this paper received support from a program designed to increase minority representation in their field of research.

[8]Department of Anatomy and Structural Biology, Albert Einstein College of Medicine, Bronx, NY 10461, USA

[9]Gruss-Lipper Biophotonic Center, Albert Einstein College of Medicine, Bronx, NY 10461, USA

[10]Integrated Imaging Program, Albert Einstein College of Medicine, Bronx, NY 10461, USA

[11]Department of Medicine, Albert Einstein College of Medicine, Bronx, NY 10461, USA

[12]Department of Urology, Albert Einstein College of Medicine, Bronx, NY 10461, USA

SUMMARY

How dedifferentiated stem-like tumor cells evade immunosurveillance remains poorly understood. We show that the lineage-plasticity regulator SOX9, which is upregulated in dedifferentiated tumor cells, limits the number of infiltrating T lymphocytes in premalignant lesions of mouse basal-like breast cancer. SOX9-mediated immunosuppression is required for the progression of *in situ* tumors to invasive carcinoma. SOX9 induces the expression of immune checkpoint B7x/B7-H4 through STAT3 activation and direct transcriptional regulation. B7x is upregulated in dedifferentiated tumor cells and protects them from immunosurveillance. B7x also protects mammary gland regeneration in immunocompetent mice. In advanced tumors, B7x targeting inhibits tumor growth and overcomes resistance to anti-PD-L1 immunotherapy. In human breast cancer, SOX9 and B7x expression are correlated and associated with reduced CD8$^+$ T cell infiltration. This study, using mouse models, cell lines and patient samples, identifies a dedifferentiation-associated immunosuppression mechanism and demonstrates the therapeutic potential of targeting the SOX9-B7x pathway in basal-like breast cancer.

Graphical Abstract

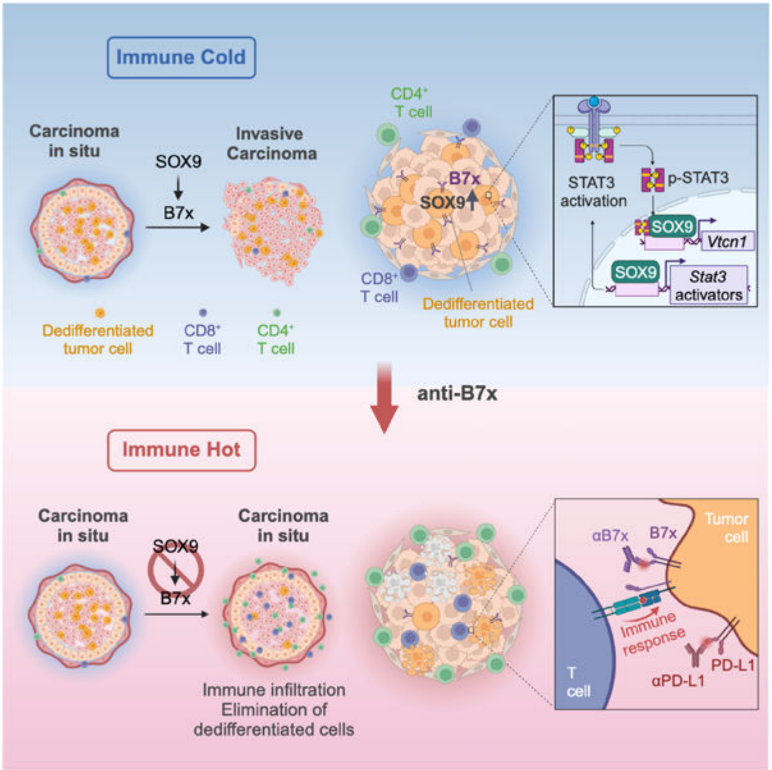

eTOC

Liu et al. demonstrate that dedifferentiated tumor cells in basal-like breast cancer rely on a regenerative program-associated pathway to evade immunosurveillance. Targeting this immunosuppressive pathway inhibits malignant progression and suppresses invasive tumor growth.

INTRODUCTION

Immune checkpoint blockade has demonstrated remarkable efficacy in some cancer types, such as melanoma and lung cancer [1–3]. In breast cancer, the combination of programmed death-ligand 1 (PD-L1) or programmed cell death protein 1 (PD-1) blocking antibodies with chemotherapy significantly improves the progression-free survival of a subset of metastatic triple-negative breast cancer (TNBC) patients [4,5]. However, most patients with breast cancer do not benefit from current immune checkpoint blockade therapy [4–6], indicating that additional mechanisms mediate immune evasion by cancer cells. A better understanding of these mechanisms is crucial for developing effective immunotherapies.

Immune-cold tumors, characterized by low tumor-infiltrating lymphocytes (TILs), are associated with poor response to immune checkpoint blockade therapy [7]. Distinct immune checkpoint molecules may regulate immune-cold tumor immune microenvironment (TIME) in different cancer types. In TNBC, increased expression of B7x (also known as B7-H4, B7S1, or VTCN1) in tumor cells is associated with the immune-cold TIME, whereas high PD-L1 in tumor cells is associated with immunoreactive microenvironment [8,9].

However, the causal role of B7x in establishing an immune-cold TIME in TNBC has not been demonstrated. B7x is a member of the B7-ligand family, which inhibits T cell proliferation and cytokine production [10,11]. Compared to other well-known B7-family ligands, such as CTLA-4 and PD-1/PD-L1, B7x is a much less studied immune checkpoint with a unique expression pattern. It is widely expressed in a broad spectrum of human neoplasms, including breast cancer, whereas it has limited expression in normal tissues [11,12]. Furthermore, increased B7x expression levels in many cancers correlate directly with tumor stage, progression, and recurrence, and inversely with TIL abundance and patient survival [8,13,14]. However, the mechanisms controlling B7x expression in cancer are not fully understood.

Breast tumorigenesis often involves the dedifferentiation of lineage-restricted progenitor cells to a multipotent state with properties of fetal mammary stem cells [15–20]. The dedifferentiated cells express a hybrid basal-luminal feature like that of fetal mammary stem cells, including co-expression of basal and luminal cytokeratin markers [21–23]. The dedifferentiation to embryonic multipotency contributes to tumor cell heterogeneity and promotes the progression of *in situ* tumor to invasive carcinoma. Emerging evidence suggests that tumor cell dedifferentiation may contribute to immune evasion [24]. However, the molecular mechanisms mediating the interaction of dedifferentiated multipotent tumor cells with TIME remain largely unclear. Of note, dedifferentiation may upregulate the expression of developmental antigens, such as cancer-testis (or oncofetal) antigens, that could trigger immune responses [24–26]. Whether dedifferentiated cells require specific strategies to overcome such immune responses is yet to be determined.

The transcription factor SOX9 is a key developmental factor that regulates functions of stem/progenitor cells in diverse epithelial tissues, including mammary stem/progenitor cells [27–29]. SOX9 acts as a pioneering factor that reprograms chromatin landscapes to drive dedifferentiation and trans-differentiation during tissue repair and carcinogenesis in multiple epithelial tissues [18,30,31]. In a mouse model of basal-like breast cancer (BLBC), a cancer subtype overlapping largely with TNBC, upregulation of SOX9 is required for dedifferentiation of the BLBC cell-of-origin luminal progenitors to multipotent-like cells. Furthermore, SOX9 is needed for the progression of mammary intraepithelial neoplasia (MIN), human ductal carcinoma *in situ* (DCIS)-like lesions, to invasive carcinoma [18]. Here, we identified an unexpected role of SOX9 in suppressing infiltrating T lymphocytes to protect dedifferentiated tumor cells from immune surveillance, thereby promoting BLBC tumor progression. We found that SOX9 upregulated B7x expression in breast cancer cells, acting through both direct transcriptional regulation and STAT3-mediated induction. Furthermore, B7x inhibition suppressed tumor growth, activated antitumor immune response, and potentiated responses to anti-PD-L1 therapy.

RESULTS

Mammary *Sox9* conditional knockout leads to massive accumulation of infiltrating T cells in MIN

Using the C3-TAg mouse model that recapitulates human BLBC [32,33], we previously showed that mammary epithelium *Sox9* conditional knockout (cKO) stalls tumor progression at a premalignant, DCIS-like MIN stage [18]. Here we found that *Sox9*-cKO (MMTV-iCre;*Sox9*$^{Fl/Fl}$;C3-TAg) MIN lesions unexpectedly contained massive lymphocytic infiltrates compared to wild-type (WT) (*Sox9*$^{Fl/Fl}$;C3-TAg) MINs (Figure 1A). These increased infiltrates were mostly CD3$^+$ T cells (Figure 1B), including both CD4$^+$ and CD8$^+$ T cells (Figure 1C and 1D). Moreover, *Sox9*-cKO lesions showed elevated levels of granzyme B$^+$ (GZMB$^+$) cells, most of which were CD8$^+$ (Figure 1E and S1A). The frequency of perforin$^+$ cells was also increased in *Sox9*-cKO lesions (Figure 1F). Spectral flow cytometry further revealed an increase of CD45$^+$ cells, CD4$^+$ T cells, CD8$^+$ T cells, and B cells in the mammary glands of *Sox9*-cKO;C3-TAg compared to WT C3-TAg mice at ~4 months of age when MIN develops, while other immune populations had no notable differences (Figure 1G, S1B and S1C). Interestingly, there were no increased lymphocytic infiltrates in mammary ducts with normal histology in *Sox9*-cKO;C3-TAg mice compared to the WT C3-TAg control, suggesting a specific role of SOX9 in suppressing infiltrating T cells in neoplastic lesions (Figure S1D).

To rule out potential effects of MMTV-iCre on infiltrating T cells, we generated MMTV-iCre;*Sox9*$^{+/+}$;C3-TAg mice as an additional WT control and compared them to MMTV-iCre;*Sox9*$^{Fl/Fl}$;C3-TAg mice generated from the same breeders. Drastically increased T cells were only observed in the *Sox9*-cKO MIN lesions but not in the *Sox9*-WT lesions expressing MMTV-iCre (Figure S1E and S1F), indicating that MMTV-iCre did not affect the frequency of infiltrating T cells. Together, these results revealed an unexpected role of epithelial SOX9 in reducing infiltrating T cells during breast tumor formation.

To further test the effect of tumor cell-expressing SOX9 on human T cell functions, we expressed SOX9 in SOX9-negative MCF7ras human breast cancer cells and cocultured them with CD4$^+$ and CD8$^+$ T cells isolated from human peripheral blood mononuclear cells (PBMCs) to assess T cell proliferation upon anti-CD3/CD28 stimulation (Figure S2A). Notably, SOX9-expressing (SOX9-OE) MCF7ras cells significantly suppressed the proliferation of both CD8$^+$ and CD4$^+$ T cells compared to the control MCF7ras cells (Figure S2B). We further assessed the effect of SOX9 overexpression in the HCC1937 TNBC cells and found it similarly suppressed the proliferation of CD8$^+$ and CD4$^+$ T cells (Figure S2C). Next, we evaluated the impact of SOX9 on antigen-specific T cell-mediated cytotoxicity utilizing MCF7ras cells because they express NY-ESO-1 and human leukocyte antigen (HLA)-A2 that can be recognized by the well-characterized HLA-A2-restricted, NY-ESO-1-specific T cell receptor (TCR) [34] (Figure S2D and S2E). We transduced human CD8$^+$ T cells with a lentiviral vector expressing the NY-ESO-1 TCR. When the engineered human CD8$^+$ T cells were cocultured with the control or SOX9-expressing MCF7ras cells, SOX9 overexpression significantly reduced T cell-mediated killing (Figure 1H). These results indicate that tumor cell-expressing SOX9 inhibits human T cell functions.

T cell depletion restores MIN progression in *Sox9*-cKO;C3-TAg mice

Sox9-cKO MIN cannot progress to invasive tumors [18]. To test whether the infiltrating T cells contribute to the inhibition of *Sox9*-cKO MIN progression, we depleted T cells in *Sox9*-cKO;C3-TAg mice starting at three months of age when MINs started to develop. To do so, mice were administered with anti-CD4 and anti-CD8 antibodies every 5 days for 2 months, which led to over 90% depletion of $CD4^+$ and $CD8^+$ T cells (Figure S2F and S2G). T cell depletion significantly accelerated invasive tumor onset in *Sox9*-cKO;C3-TAg mice (Figure 1I). We previously showed that tumors in *Sox9*-cKO;C3-TAg mice can only develop from “escapee” cells that fail to excise the floxed *Sox9* allele [18]. Interestingly, in T cell-depleted mice, over 50% of tumors were SOX9-negative, suggesting they were developed from *Sox9*-null cells, whereas all tumors in isotype control mice were still developed from *Sox9*-replete escapees (Figure 1J). Intriguingly, T cell depletion in *Sox9*-WT;C3-TAg mice did not accelerate tumor development (Figure S2H), suggesting that *Sox9*-WT MINs are sufficiently immunosuppressed as indicated by very low T cell infiltration in these lesions. These data suggested that SOX9-mediated suppression of T cell immunity plays a key role in enabling the progression of premalignant lesions to invasive tumors.

SOX9 upregulates immune checkpoint molecule B7x

By comparing the transcriptomes between *Sox9*-WT and *Sox9*-cKO ER^- luminal cells, a cell-of-origin for BLBC [35,36], we found that *Vtcn1* (encoding B7x) was one of the top differentially expressed genes and the only immune checkpoint that was significantly downregulated in *Sox9*-cKO cells (Figure 2A and S3A). Furthermore, we observed that B7x protein was substantially downregulated in the *Sox9*-cKO;C3-TAg MINs compared to the WT control (Figure 2B). We also assessed the association of SOX9 and B7x expression in invasive tumors developed spontaneously in the C3-TAg mouse model crossed to *Sox9* enhancer/promoter-driven GFP (*Sox9*-GFP) transgenic reporter mice [18]. B7x expression was substantially increased in *Sox9*-GFP^+ compared to *Sox9*-GFP^- tumor cells, and the frequency of $B7x^+$ cells was also higher in the *Sox9*-GFP^+ than *Sox9*-GFP^- population (Figure 2C, S3B and S3C). Furthermore, within *Sox9*-GFP^+ cells, B7x levels were higher in *Sox9*-GFP^{high} than *Sox9*-GFP^{low} cells (Figure S3D). The expression of other immune checkpoint molecules, including PD-L1 and B7-H3, did not show a consistent correlation with *Sox9*-GFP levels (Figure 2C and S3D).

In human breast cancer, B7x is elevated in tumors with an “immune-cold” microenvironment [8,9]. However, the regulation of B7x expression and its function in breast cancer is still poorly defined. To further investigate if SOX9 activates B7x expression, we overexpressed SOX9 in SOX9 and B7x-negative MCF7ras cells using a doxycycline-inducible vector and observed a robust induction of total and cell-surface B7x protein upon SOX9 overexpression (Figure 2D and 2E). Furthermore, SOX9 overexpression in the TNBC cell line HCC1937, which expresses a moderate level of B7x, also dramatically upregulated B7x expression (Figure S3E and S3F). Conversely, SOX9 knockdown in B7x-positive SK-BR3, MDA-MB-468, and HCC1937 human breast cancer cells downregulated B7x mRNA (Figure S3G–S3I) and protein levels (Figure 2F and 2G). These data demonstrate that SOX9 is a key activator of B7x expression in multiple breast cancer cell lines.

B7x acts downstream of SOX9 to suppress infiltrating T cells in MIN and promote invasive tumor onset

To assess whether B7x contributes to immune suppression during BLBC progression, we crossed C3-TAg mice with $B7x^{-/-}$ mice [37,38]. $B7x^{-/-}$;C3-TAg (B7x-KO) mice showed significantly delayed tumor onset compared to $B7x^{+/+}$;C3-TAg (B7x-WT) mice (Figure 3A).

B7x-KO also led to significantly increased $CD3^+$ T cells in MIN lesions, including both $CD4^+$ and $CD8^+$ T cells (Figure 3B–3D), indicating that B7x-KO phenocopies *Sox9*-cKO in increasing tumor-infiltrating T cells in early BLBC tumors. After invasive tumor onset, B7x-KO tumors grew at a similar rate as B7x-WT tumors (Figure S4A). There was also no significant difference in the frequency of $CD8^+$ and $CD4^+$ T cells between B7x-WT and -KO invasive tumors (Figure S4B and S4C). Interestingly, while MIN lesions expressed very little PD-L1, invasive tumors of both genotypes expressed substantial PD-L1 (Figure S4D).

We further investigated if B7x overexpression can rescue the *Sox9*-cKO phenotype. To do so, we transduced *Sox9*-cKO;C3-TAg mammary organoids with a B7x lentiviral vector (Figure S4E) and transplanted them into REAR mice, which are a C3-TAg subline that does not develop spontaneous tumors but is immunologically tolerant to SV40 T-antigen [39]. Notably, B7x overexpression significantly accelerated tumor onset by *Sox9*-cKO;C3-TAg organoids (Figure 3E). Moreover, B7x overexpression reduced $CD8^+$ T cells and increased T_{reg} cells in *Sox9*-cKO MINs (Figure 3F, S4F and S4G), suggesting that B7x overexpression re-established an immunosuppressed microenvironment in *Sox9*-deficient MINs.

We also examined whether B7x upregulation mediated the suppression of T cell cytotoxicity by SOX9-overexpressing human cancer cells as shown above (Figure 1H). We treated the coculture of MCF7ras and NY-ESO-1 TCR-expressing T cells with a B7x blocking antibody (H19). Interestingly, anti-B7x treatment significantly restored the T cell-mediated cytotoxicity toward SOX9-expressing tumor cells, whereas it did not affect the cytotoxicity toward the control SOX9-negative tumor cells that did not express B7x (Figure 3G). Together, our results demonstrate that B7x upregulation by SOX9 suppresses the abundance of infiltrating T cells and their activity.

B7x is upregulated in dedifferentiated tumor cells in MIN

We previously showed that, during C3-TAg BLBC tumorigenesis, a small population of ER^- luminal cells upregulate SOX9, and these $SOX9^{high}$ cells co-express basal (K14) and luminal (K8) keratins [18]. Transcriptomic profiling and ATAC-seq demonstrated that these $SOX9^{high}K8^+K14^+$ cells upregulate the basal-cell gene signature and gain the chromatin landscape of basal cells, thus acquiring a hybrid luminal-basal phenotype [18]. Here, we further showed that $SOX9^{high}$ cells significantly upregulated a set of embryonic multipotent progenitor (EMP)-specific genes identified previously [23] (Figure 4A). Furthermore, single-cell RNA-seq comparing normal and MIN-containing C3-TAg mammary glands demonstrated that a cluster of ER^- luminal cells in C3-TAg glands co-express luminal and basal markers, and that these cells express multiple EMP-unique genes (Figure 4B and S5A). Together, these results suggest that $K8^+K14^+$ cells are dedifferentiated cells with EMP properties [18]. Formation of similar $K8^+K14^+$ multipotent cells is also found in other mammary tumor models [15–17,19]. However, how these cells may engage with tumor immune microenvironment remains unclear. Thus, we investigated whether the SOX9-B7x axis was involved in protecting the dedifferentiated cells from immune surveillance.

The *Sox9*-GFP;C3-TAg premalignant mammary glands showed increased frequency of $B7x^+$ cells in *Sox9*-GFP^+ than *Sox9*-GFP^- luminal cells (Figure S5B and S5C). Among *Sox9*-GFP^+ luminal cells, which were nearly entirely ER^- (Figure S5D), B7x expression was markedly higher in the *Sox9*-GFP^{high} cells compared to GFP^{low} cells in C3-TAg mice (Figure 4C). Agreeing with that *Sox9*-GFP^{high} cells were enriched in K8^{+}K14^{+} dedifferentiated cells (Figure 4A and 4B) [18], the K8^{+}K14^{+} MIN cells expressed significantly higher levels of B7x than K8^{+}K14^{-} cells (Figure 4D and S5E). Immunostaining of FACS-sorted B7x^{+} and B7x^{-} cells from C3-TAg mammary epithelial organoids also showed that B7x^{+} cells were significantly enriched in K8^{+}K14^{+} cells compared to B7x^{-} cells (Figure 4E and S5F). To determine the involvement of the SOX9-B7x pathway in dedifferentiation in other tumor models, we utilized a *Pik3ca*^{H1047R}/*p53*^{null} mammary organoid transplantation-based tumor model [40], as these mutations cause dedifferentiation in the mammary gland [15,19]. In early tumor lesions of this model, we found that K8^{+}K14^{+} cells expressed significantly higher levels of SOX9 and B7x than K14 or K8 single-positive cells (Figure S5H and S5I). Together, these results support that the SOX9-B7x pathway is upregulated in dedifferentiated tumor cells in various murine mammary tumor models.

Dedifferentiated cells require B7x to evade immunosurveillance

To investigate if B7x is functionally involved in the accumulation of dedifferentiated cells, we analyzed MIN lesions in B7x-WT and B7x-KO C3-TAg mice. While B7x perturbation did not affect MIN numbers (Figure S5J), the percentage of MIN lesions that contained K8^{+}K14^{+} cells was significantly reduced in B7x-KO C3-TAg mice, along with the reduction of K8^{+}K14^{+} cell frequency within each lesion (Figure 4F). Conversely, B7x overexpression in *Sox9*-cKO MINs led to an increased K8^{+}K14^{+} MIN frequency and elevated K8^{+}K14^{+} cell numbers within MINs (Figure 4G). These data indicated that B7x facilitates the accumulation of dedifferentiated cells during BLBC tumorigenesis. The *Sox9*-cKO;C3-TAg MIN lesions have diminished K8^{+}K14^{+} dedifferentiated cells [18]. To test whether infiltrating T cells in the *Sox9*-cKO lesions contributes to the elimination of these dedifferentiated cells, we depleted T cells using anti-CD4 and -CD8 antibodies as done in Figure 1I. T cell depletion in *Sox9*-cKO;C3-TAg mice led to an increase of MIN lesions containing K8^{+}K14^{+} cells as well as more frequent K8^{+}K14^{+} cells within each lesion (Figure 4H and S5J). Collectively, these data suggest that the SOX9-B7x axis is required for establishing an immunosuppressive microenvironment to protect dedifferentiated tumor cells from immunosurveillance.

Since tissue regeneration often involves dedifferentiation of committed cells [41,42], we asked whether B7x-mediated immunosuppression is required for mammary gland regeneration. We established mammary organoid cultures from WT or B7x$^{-/-}$ BALB/c mice, which had similar organoid-forming efficiency (Figure S5K). We then transplanted each type of organoids to cleared mammary fat pads of WT or Rag1$^{-/-}$ BALB/c mice. As expected, WT organoid cells efficiently regenerated mammary ductal trees in both WT and Rag1$^{-/-}$ recipient mice. However, B7x$^{-/-}$ cells can only regenerate ductal trees in immunodeficient Rag1$^{-/-}$ but not in immunocompetent WT mice (Figure 4I). These results suggest that, while B7x is not required for the cell-intrinsic regenerative potential, it is essential for protecting regenerating cells from immune surveillance. We previously showed that ectopic SOX9 expression in normal mammary epithelial cells induces their dedifferentiation to acquire multipotent gland-reconstituting activity [27]. Interestingly, SOX9 overexpression substantially induced B7x expression in normal basal and luminal cells (Figure S5G). These results suggest that the SOX9-B7x axis is part of tissue regeneration program for protecting dedifferentiated cells from immunosurveillance.

SOX9 upregulates B7x through activating the STAT3 pathway and direct binding to the B7x gene locus

Next, we investigated the molecular mechanism by which SOX9 activates B7x expression. Gene Set Enrichment Analysis (GSEA) comparing *Sox9*-WT and *Sox9*-cKO ER^- luminal cell transcriptomes showed that STAT3 signatures were significantly downregulated in *Sox9*-cKO cells (Figure S6A). We tested the involvement of STAT3 in SOX9-induced B7x upregulation using SOX9 and B7x-negative MCF7ras cells. We found that SOX9 overexpression led to robust activation of STAT3 as shown by phosphorylation at Tyr705 (p-STAT3), as well as a moderate increase of total STAT3 protein and mRNA levels (Figure 5A and S6B). SOX9 also increased JAK activation, as measured by phospho-JAK1/2 levels (Figure 5B). Furthermore, JAK inhibitor Ruxolitinib suppressed SOX9-induced STAT3 activation, suggesting SOX9 activates the JAK-STAT3 pathway (Figure S6C). SOX9 overexpression in mouse TNBC cell line 4T1 also led to STAT3 activation and increased B7x expression (Figure S6D). Moreover, while the *Sox9*-WT C3-TAg MIN lesions showed robust STAT3 activation, the p-STAT3 level in *Sox9*-cKO lesions was significantly diminished (Figure 5C). These data suggest that SOX9 expression leads to STAT3 activation both *in vitro* and *in vivo*.

The IL6-STAT3 pathway has been implicated in regulating B7x expression in microglia [43]. Hence, we evaluated the potential role of STAT3 in B7x induction by SOX9. We treated SOX9-overexpressing MCF7ras cells with the STAT3 inhibitor Stattic, which selectively blocks the function of the STAT3 SH2 domain, thereby inhibiting STAT3 [44]. As predicted, Stattic treatment diminished the induction of B7x by SOX9 (Figure 5D). A similar attenuating effect was observed in the TNBC cell line MDA-MB-468 (Figure 5E) and mammary tumor organoids derived from C3-TAg mice (Figure 5F). To exclude the potential off-target effect of Stattic, we further used CRISPR/Cas9 to knock out *STAT3* in SOX9-overexpressing MCF7ras cells, which led to diminished B7x induction by SOX9 (Figure 5G). Furthermore, treating MCF7ras cells with STAT3-activating IL6 family cytokines markedly increased B7x expression (Figure 5H). Taken together, these results show that SOX9 upregulates B7x through STAT3 activation.

To identify the direct transcriptional targets of SOX9 that is linked to STAT3 signaling and B7x expression, we performed SOX9 ChIP-seq in MCF7ras cells ectopically expressing SOX9. Interestingly, SOX9 showed significant binding on the promoters and gene bodies of both *VTCN1* (encoding B7x) and *STAT3* (Figure 5I). ChIP-qPCR validated SOX9 occupancy in these regions (Figure S6E). The direct binding of SOX9 to *VTCN1* and *STAT3* genes was similarly observed in MDA-MB-468 cells by endogenous SOX9 ChIP-qPCR (Figure S6F). We next applied Enrichr analysis [45] to search for significantly enriched gene signatures in the SOX9 ChIP-seq peaks. Notably, it showed that SOX9 peaks had enrichment of over 1000 STAT3 targets in the ChEA 2016 datasets [46] (Figure S6G). HOMER analysis [47] also revealed an enrichment of the STAT3 motif in the SOX9 binding peaks (Figure S6H), indicating potential co-occupancy of SOX9 and STAT3 to some of the target genes.

To confirm this, we compared the SOX9 ChIP-seq data with previously published STAT3 and p-STAT3 ChIP-seq data in MCF7 cells treated with IL6 or PBS[48]. Interestingly, when the STAT3 pathway is activated by IL6, STAT3/p-STAT3 occupied the same loci as SOX9 on *VTCN1* and *STAT3* genes (Figure 5I). Moreover, at the genome-wide level, 16% of SOX9-binding peaks are also occupied by STAT3 (Figure 5J). These results suggest that SOX9 acts in concert with STAT3 to regulate gene expression of a significant fraction of the SOX9 targets, including *VTCN1*.

SOX9 upregulates multiple STAT3 activators

We also compared the control and SOX9-expressing MCF7ras cells by RNA-seq analysis. Ingenuity Pathway Analysis (IPA) identified STAT3 and its activators (JAK1, JAK2, OSM, IL11, and LIF) as significant upstream regulators in SOX9-expressing cells (Figure S6I). In addition, multiple STAT3 activators, including IL6ST, JAK1, OSMR, IL6R, LIFR and LIF [49], were also upregulated by SOX9 overexpression in MCF7ras cells (Figure S6J). Consistently, these activators were significantly downregulated in *Sox9*-cKO ER^- luminal cells *in vivo* (Figure S6K). The upregulation of LIF by SOX9 was also confirmed by ELISA (Figure S6L). Furthermore, SOX9 occupied the promoters and gene bodies of these STAT3 activators in SOX9-expressing MCF7ras cells (Figure S6M). ChIP-qPCR in MDA-MB-468 cells confirmed that the endogenous SOX9 also bound to the gene loci of multiple STAT3 upstream regulators (Figure S6N), suggesting that SOX9 directly upregulates the expression of multiple STAT3 activators, leading to robust STAT3 activation.

Targeting B7x activates anti-tumor immunity and sensitizes response to anti-PD-L1 treatment

To investigate the therapeutic efficacy of targeting the SOX9-B7x axis in breast cancer models, we isolated primary tumor cells from spontaneous C3-TAg tumors and orthotopically transplanted them into 6–8 weeks old immunocompetent REAR mice to generate allograft tumors. Once tumors reached 3–4 mm in diameter, recipient mice were treated with isotype control or anti-mouse B7x monoclonal antibody 1H3 [50] (Figure 6A). Anti-B7x treatment significantly suppressed the growth of allografts generated from three different C3-TAg spontaneous tumors (Figure 6B). Flow cytometry analysis revealed that anti-B7x treatment significantly increased tumor-infiltrating $CD45^+$ immune cells, $CD3^+$ T cells, and effector $CD4^+$ T cells but reduced the percentage of $FOXP3^+$ T_{reg} cells (Figure 6C, S7A and S7B). $CD8^+$ T cells were also trending higher in the anti-B7x treatment group, while myeloid cell populations remained unchanged (Figure S7B). We further tested the efficacy of anti-B7x in orthotopic tumors generated by *Pik3ca*^{H1047R}/*p53*^{null} mammary organoids in FVB/N mice and found that anti-B7x treatment significantly reduced tumor growth and increased the frequency of $CD8^+$ and $GZMB^+$ cells (Figure 6D and 6E), although the frequencies of effector $CD4^+$ T cells and T_{reg} cells were not significantly changed (Figure S7C). The distinct immune cell changes caused by anti-B7x treatment in different tumor models are likely due to the heterogenous immune microenvironment in these tumors. It is not uncommon that different tumor models of the same cancer type can respond differently to the same immune checkpoint blockade. For example, both MC38 and CT26 are mouse colon cancer tumor lines, but they respond differently to immune checkpoint inhibitors [51].

Only a small percentage of TNBC patients respond to the anti-PD-L1 treatment [4]. We therefore investigated whether B7x knockout can improve the efficacy of anti-PD-L1 blocking antibody in C3-TAg spontaneous BLBC tumors. When B7x-WT or B7x-KO C3-TAg tumors reached 3–5 mm in diameter, mice were treated with anti-PD-L1 or isotype control every three days for four doses (Figure 6F). The B7x-WT C3-TAg tumors were completely refractory to anti-PD-L1. Remarkably, anti-PD-L1 significantly inhibited tumor growth in B7x-KO C3-TAg mice (Figure 6G). Furthermore, we noticed that anti-PD-L1 treatment resulted in a durable response in most B7x-KO mice after treatment ended (Figure S7D). Consistent with the inhibitory effect on tumor growth, anti-PD-L1 treatment increased the tumor-infiltrating $CD8^+$ T cells, $GZMB^+$ cells, and effector $CD4^+$ T cells in B7x-KO tumors, but not in B7x-WT tumors (Figure 6H and S7E). The frequency of T_{reg} cells in $CD4^+$ T cells were also reduced by anti-PD-L1 in B7x-KO tumors (Figure 6H and S7F). Taken together, these results suggest that B7x targeting can inhibit BLBC tumor growth and enhance the efficacy of anti-PD-L1 immunotherapy.

SOX9 and B7x expression are correlated in cancer cells and associated with reduced $CD8^+$ T cell infiltration in human breast cancer

We evaluated the expression of SOX9 and B7x in human DCIS and the correlation of these proteins with the level of T cell infiltration in a cohort of 20 DCIS cases. We co-stained SOX9 and B7x using fluorophore-conjugated anti-SOX9 and B7x antibodies and performed CD8 IHC on the consecutive sections. We found a significant correlation of SOX9 and B7x expression at the individual DCIS cell level, as well as among DCIS cases (Figure 7A). Furthermore, SOX9 and B7x expression levels showed inverse correlations with the density of infiltrating CD8 T cells in DCIS cases (Figure 7A). These results support the role of the SOX9-B7x axis in controlling T cell infiltration in human DCIS.

We then investigated the correlation of the SOX9-B7x axis with T cell infiltration in human invasive breast cancer. We measured the expression of SOX9, B7x, p-STAT3, pan-CK, CD4, and CD8 by Opal 7-color multiplex IF on a tissue microarray that contains 95 cases of invasive breast carcinoma. Notably, we observed a positive correlation of SOX9, B7x and p-STAT3 levels in pan-CK^+ cancer cells at the single-cell level either in all cases or only TNBC (Figure 7B and S8A). We next measured the correlation between B7x or SOX9 and the frequency of tumor-infiltrating T cells among TMA cases. B7x expression showed a negative trend with the frequency of $CD8^+$ T cells (Figure 7C), consistent with previous studies showing the association of B7x with immune-cold phenotypes in breast cancer [8,9]. SOX9 expression was not negatively correlated with $CD8^+$ T cell infiltration when all the samples in TMA were analyzed. However, we noted that SOX9 expression had a bimodal distribution, with ~50% TMA cases clustering around very low H scores (0–10) (Figure S8B). Interestingly, when only cases with SOX9 H score ≥ 11 were analyzed, SOX9 expression showed a significantly negative correlation with $CD8^+$ T cell infiltration (Figure 7C). A similar negative correlation between SOX9 H score and $CD8^+$ T cells was found among TNBC cases in the TMA cohort (Figure S8B). We did not observe a significant association between B7x or SOX9 and $CD4^+$ T cells in this TMA cohort.

We also evaluated the correlation of SOX9, B7x and STAT3 expression in a published scRNA-seq dataset containing 10 TNBC cases (GSE176078) [52]. We found there is a significant correlation between SOX9 and B7x levels among tumor cells (Figure 7D). The correlation between STAT3 and SOX9 or B7x was weaker, likely due to that STAT3 activity is mainly regulated by protein phosphorylation rather than at mRNA level. Interestingly, SOX9-high TNBC cells also upregulated *KRT14* and the EMP genes associated with dedifferentiation in the C3-TAg model (Figure 7E).

Using the Cancer Genome Atlas (TCGA) bulk RNA-seq dataset, we found that *VTCN1* was expressed at higher levels in the basal-like subtype than other subtypes (Figure S8C), similar to *SOX9* [18]. *VTCN1* expression was significantly higher in *SOX9*-high tumors (Figure S8D). Moreover, GSEA results revealed that JAK/STAT signaling was enriched in $SOX9^{high}$ or $VTCN1^{high}$ TCGA BRCA tumors (Figure S8E). These data further support a correlation between SOX9 and B7x expression and STAT3 activation in human breast cancer. TIMER (Tumor Immune Estimation Resource) analysis [53] of BLBC samples in the TCGA dataset showed a negative correlation between the expression of *SOX9*, *B7x* and *STAT3* and the infiltration levels of the Th1 effector $CD4^+$ T cells (Figure S8F). B7x expression was negatively correlated with naïve $CD8^+$ T cells as well (Figure S8F). Taken together, these results support the relevance of the SOX9-B7x pathway in immunosuppression in human breast cancer.

DISCUSSION

Cancer utilizes diverse mechanisms to suppress anti-tumor immunity, leading to limited responses to current immune checkpoint blockade therapy that primarily targets the CTLA-4 and PD-1/PD-L1 pathways [7,54]. Better understandings of the diverse mechanisms regulating tumor immune microenvironment (TIME) are needed for developing new immunotherapy strategies and tailoring treatments for individual patients. Here, we uncovered a cell dedifferentiation-associated mechanism for establishing immune-cold TIME that safeguards dedifferentiated tumor cells and drives tumor progression. We found that the stem/progenitor transcription factor SOX9, a lineage plasticity driver promoting dedifferentiation in BLBC, upregulated the expression of the immune checkpoint B7x to suppress infiltrating T lymphocytes, which in turn protected dedifferentiated tumor cells from immune surveillance. Immune evasion mediated by the SOX9-B7x pathway promotes the progression of non-invasive lesions to invasive tumors. Furthermore, targeting B7x in BLBC tumors activated the antitumor response, suppressed tumor growth, and conferred sensitivity to anti-PD-L1 treatment. These results uncovered a mechanism coupling tumor cell dedifferentiation and immune escape and revealed an immunological vulnerability of dedifferentiated BLBC tumor cells (Figure S8G).

Dedifferentiation of committed progenitor cells to an embryonic-like multipotent state contributes to the formation of invasive tumors and tumor cell heterogeneity in breast cancer [15–19,55]. Similar processes also play a key role in other cancer types, such as pancreatic and skin cancer [30,31,56,57]. Strategies targeting these dedifferentiated tumor cells will help cancer prevention and treatment. It is largely unclear how dedifferentiated cells interact with the host immune system [24]. Here we found that dedifferentiated tumor cells express high levels of SOX9 and B7x and utilize this pathway to limit infiltrating T cells and evade immunosurveillance. Thus, the lineage plasticity driver SOX9 can concomitantly promote dedifferentiation and upregulate immune checkpoints to enable immunoevasion. We also found B7x was required for normal mammary gland regeneration in immunocompetent hosts. This suggests that the mechanisms protecting dedifferentiated cells from immune surveillance are likely evolved for facilitating tissue regeneration, in which committed cells often dedifferentiate into facultative stem cells with embryonic features to mediate tissue repair [41,42,58]. The antigen(s) in dedifferentiated cells that elicit the immune response remain to be determined. One possibility is that, while gaining embryonic-like multipotency, these cells also upregulate certain cancer-testis antigens that are immunogenic [24–26].

SOX9 plays a crucial role in the initiation and progression of multiple cancer types [59,60]. However, mechanisms by which SOX9 promotes aggressive tumor phenotypes are still poorly understood. Previous work showed that SOX9 acts as a pioneer factor to reprogram cell-intrinsic stem/progenitor cell potentials [30]. Our current work uncovered an unexpected cell-extrinsic function of SOX9 in suppressing adaptive anti-tumor immunity, linking tumor cell dedifferentiation programs to TIME regulation. We demonstrated that the cell-extrinsic function of SOX9 on TIME played a prominent role in driving BLBC progression, as evidenced by the result that T cell depletion could rescue MIN progression in *Sox9* knockout C3-TAg animals. Supporting the role of SOX9-mediated immunosuppression in BLBC progression, the progression of *in situ* tumor to invasive carcinoma in humans is accompanied by the transition to a more suppressive TIME [61,62]. SOX9-mediated regenerative programs can also regulate innate immune response. In lung cancer metastasis, shift towards a SOX9^{high} regenerative state confers resistance to natural killer cells and enables macro-metastasis formation [63,64]. Together, these data demonstrate a multifaceted role of SOX9 in regulating both innate and adaptive tumor immune microenvironment.

B7x has limited expression in normal tissues but is upregulated in various cancer types through still poorly defined mechanisms [65]. A previous study showed that STAT3 activation upregulates B7x expression in microglia and macrophages [43]. We identified that SOX9 activated B7x expression through both direct binding to the *VTCN1* locus and activation of the STAT3 pathway. SOX9 upregulated multiple activators in the STAT3 pathway, leading to potent activation of p-STAT3. Both SOX9 and p-STAT3 bind to the regions near the B7x transcription start site, suggesting they act cooperatively to induce B7x expression. Interestingly, 16% of SOX9 binding sites in the genome were co-occupied by STAT3, suggesting the broad cooperation of SOX9 and STAT3 in regulating target gene expression. STAT3 is an important cancer signaling pathway regulating diverse processes of cancer pathogenesis [66,67]. Our study uncovered a role of lineage plasticity program in regulating the STAT3 pathway and B7x expression in breast cancer. In agreement with the role of SOX9-STAT3-B7x in establishing immune-suppressive TIME, STAT3 knockout in the polyoma middle T tumor model leads to increased T cell recruitment [68].

Less than 20% of pre-selected PD-L1$^+$ TNBC responds to anti-PD-L1 / anti-PD1 immunotherapy [4,5]. The immune-cold tumor microenvironment is a major contributing factor to poor clinical responses to immune checkpoint blockade therapy [7]. Interestingly, B7x expression, but not PD-L1, has been shown to correlate with immune-cold tumor phenotypes in TNBC [8,9], although a causal role of B7x in immune-cold tumors has not been shown. Using the B7x knockout and rescue mouse models, we demonstrated that B7x indeed inhibited infiltrating T cells in C3-TAg tumors and accelerated tumor progression. It is well-established that B7x can inhibit the inflammatory cytokine production and the proliferation of $CD4^+$ and $CD8^+$ T cells, which was likely to suppress the abundance and function of infiltrating T cells [10,65]. Importantly, B7x knockout greatly improved the response to anti-PD-L1 treatment in otherwise refractory C3-TAg tumors. Furthermore, anti-B7x monotherapy markedly reduced the growth of C3-TAg and other murine tumor models. Together, our results established a causal role of the SOX9-B7x pathway in generating immune-cold TIME and demonstrated that B7x is a promising immunotherapy target in breast cancer.

Limitations of Study

While we have shown that SOX9 promotes DCIS progression through suppressing T cell responses, the specific involvement of $CD8^+$, $CD4^+$, or both T cell subsets in controlling DCIS progression remains to be determined. Additionally, understanding which types of BLBC tumors are more sensitive to B7x inhibition and whether higher B7x or SOX9 expression levels correlate with treatment responsiveness is crucial for tailored therapeutic approaches. This can be helped by analyzing a larger cohort of BLBC/TNBC human samples for B7x and SOX9 expression and T cell infiltration. Finally, further investigation is needed to explore the role of the SOX9-B7x pathway in non-BLBC cancer subtypes. While our in vitro data showed that SOX9 can induce B7x expression in luminal and Her2-overexpression breast cancer cell lines, whether this pathway is involved in immunosuppression in these cancer subtypes *in vivo* requires further investigation.

STAR METHODS

RESOURCE AVAILABILITY

Lead contact

- Further information and requests for resources and reagents should be directed to the lead contact, Wenjun Guo (Wenjun.guo@einsteinmed.edu).

Materials availability

- This study did not generate new unique reagents.

Data and code availability

- The raw data and processed data for RNA-seq, ChIP-seq, and single-cell RNA-seq have been deposited in GEO SuperSeries GSE219110. Published microarray data were downloaded from GEO: GSE135892. Published ChIP-seq data of MCF7 cells used in this study are available from GEO: GSE126004. Public scRNA-seq data of human breast cancer patients used in this study are available from GEO: GSE176078.
- This paper does not report original code.

- Any additional information required to reanalyze the data reported in this paper is available from the lead contact upon request.

EXPERIMENTAL MODEL AND STUDY PARTICIPANT DETAILS

Mice—All experiments were performed under protocols approved by the Institutional Animal Care and Use Committee of Albert Einstein College of Medicine. MMTV-iCre and *Sox9*-GFP mice were obtained as previously described [18]. C3-TAg (JAX # 013591), Sox9$^{Fl/Fl}$ (JAX # 013106) and C3-TAg REAR (JAX #030386) Rag1$^{-/-}$ mice (JAX #002216) were obtained from the Jackson Laboratory (Bar harbor, ME). MMTV-iCre;*Sox9*$^{Fl/Fl}$;C3-TAg and *Sox9*$^{Fl/Fl}$;C3-TAg mice were backcrossed to FVB/NJ for 6 generations and generated as littermates. *Sox9*-GFP;C3-TAg mice were backcrossed to FVB/NJ for at least 10 generations. MMTV-iCre;*Sox9*$^{+/+}$;C3-TAg mice were generated by crossing MMTV-iCre;*Sox9*$^{Fl/+}$ with *Sox9*$^{Fl/+}$;C3-TAg mice. B7x$^{-/-}$ mice (BALB/c background) were obtained as previously described [50]. B7x$^{-/-}$;C3-TAg mice in a BALB/c x FVB/NJ mixed background were generated by crossing B7x$^{-/-}$ with C3-TAg mice. Mice were housed in individual cages with access to food and water ad libitum at a specific pathogen-free barrier facility under a 12-hour light/12-hour dark cycle.

Human samples—FFPE sections of 20 human DCIS cases were obtained from archival tissue bank of Montefiore Einstein Cancer Center in accordance to Einstein IRB approval (#13-01-048). The breast cancer tissue microarray was purchased from US Biomax (BR1902) with Einstein IRB approval (2018–9307).

Cell culture and treatment—MCF7ras, SK-BR3, MDA-MB-468 were cultured in Dulbecco's Modified Eagle Medium (DMEM, Corning) with 10% FBS (VWR). 4T1 and HCC1937 cells were cultured in RPMI1640 medium (Gibco) containing 10% FBS. MCF7ras tetO-SOX9, HCC1937 tetO-SOX9, and 4T1 tetO-SOX9 cells were generated as described [27]. To induce SOX9 expression, tetO-SOX9 cells were treated with 2 μg/ml doxycycline (Sigma-Aldrich, D9891) for 3 days. For Stattic treatment, MCF7ras tetO-SOX9 cells, MDA-MB-468 cells, and C3-TAg tumor organoids were treated with Stattic (Cayman Chemical Company, 14590) at indicated concentrations for 3 days. For recombinant IL6-family cytokine treatment, MCF7ras Ctrl cells were seeded in culture for overnight and then treated with 50 ng/ml OSM (R&D Systems, 295-OM-010cf), LIF (BioLegend, 593902), or IL6 (BioLegend, 570802) for 2 days. For Ruxolitinib treatment, MCF7ras tetO-SOX9 cells were seeded in culture for overnight and then treated with Ruxolitinib (Cayman Chemical Company, 11609) at indicated concentrations for 3 days.

Mammary organoid culture—Murine mammary epithelial organoids and mammary tumor organoids were cultured as previously described [69,70]. Briefly, cells were cultured in Advanced DMEM/F12 medium (Life Technology) supplemented with 5% heat-inactivated FBS (Sigma, F2442), 10 ng/ml EGF (Sigma, E9644), 20 ng/ml FGF2 (EMD Millipore, GF003), 4 mg/ml Heparin (Sigma, H4784), 5 μM Y-27632 (Cayman Chemical Company, 10005583–10) and 5% Matrigel (Corning, 354234) on 2-hydroxyethyl methacrylate (Poly-HEMA) coated 6-well plates (2 × 10^5 cells / well). Organoids were washed with cold PBS and dissociated with 0.05% Trypsin-EDTA for passaging every 3–4 days. For organoid-forming assay, 200 cells/well were seeded in ultra-low attachment 96-well plates (Corning, 07200603) with organoid medium, organoids more than 100 µm in diameter were counted after 7-day culture.

METHOD DETAILS

Lentiviral vectors and CRISPR/Cas9 Editing—Lentivirus was prepared as described previously [18]. The *SOX9* shRNAs were cloned in the pLKO.1-puro lentiviral vector as described previously [27]. The sgRNA targeting *STAT3* gene was designed using the CHOPCHOP webserver [71] and cloned into the lentiCRISPRv2-blast (Addgene #83480, a gift from Mohan Babu). The sgRNA targeting sequences are: sgSTAT3 - GTCAGGATAGAGATAGACCAG, sgNT - GCGAGGTATTCGGCTCCGCG. Cells were transduced with the vectors and then selected with blasticidin (Corning).

Immunohistochemistry, immunofluorescence, and imaging quantification—Formalin-fixed and paraffin-embedded tissue sections were processed and stained with the standard protocol described previously [18]. The following primary antibodies were used: anti-CD3 (1:200, Fisher Scientific, RM9107S0), anti-CD4 (1:100, Cell Signaling Technology, 25229S), anti-human CD8 (1:200, Cell Signaling Technology, 85336S), anti-CD8 (1:200, Cell Signaling Technology, 98941S), anti-Granzyme B (1:200, Cell Signaling Technology, 44153S), anti-perforin (1:50, Cell Signaling Technology, # 31647), anti-FOXP3 (1:50, eBioscience, #14-5773-82), anti-SOX9 (1:200, Cell Signaling Technology, 82630S), anti-B7x (1:200, Cell Signaling Technology, 14572S), anti-PD-L1 (1:100, eBioscience, #14-5982-82), anti-Keratin 8 (1:80, Developmental Studies Hybridoma Bank, AB_531826), anti-Keratin 14 (1:800, BioLegend, 905304), and anti-Keratin 14 (1:400, BioLegend, 906004). For immunofluorescence staining, the following fluorophore conjugated secondary antibodies were used at 1:200 or 1:400: anti-rabbit IgG AF647 (Jackson ImmunoResearch, 111-605-144), anti-rat IgG AF568 (Invitrogen, A-11077), anti-mouse IgG AF568 (Invitrogen, A-11031), anti-goat AF568 (Invitrogen, A-11057), anti-chicken IgY AF488 (Jackson ImmunoResearch, 103-545-155).

For immunohistochemistry, the ImmPRESS HRP goat anti-rabbit IgG Polymer Reagent (Vector Laboratories, MP-7401) and ImmPRESS HRP goat anti-rat IgG Polymer Reagent (Vector Laboratories, MP-7404) were used. HRP signal was developed using DAB Peroxidase (HRP) Substrate Kit (Vector Laboratories, SK-4100). DAB exposure time was determined when positive control slides showed desirable staining intensity while the negative control (IgG or no primary Ab) showed limited background. All samples in the same experiments were developed with the same DAB exposure time and counterstained with hematoxylin identically. Immunohistochemistry slides were scanned with a P250 High-Capacity Slide Scanner (3DHISTECH). Representative images were captured by CaseViewer (3DHISTECH) and imported to ImageJ (FIJI) [72] blinded to sample information. After color deconvolution into hematoxylin and DAB channels using “H DAB” function, the same threshold was applied to all images to identify the regions of interest and count number of positive cells. In regions of interest, IntegrateDensity of specific proteins was measured and normalized to hematoxylin$^+$ area for measuring expression levels, positive cell counts were measured and normalized to total hematoxylin$^+$ area or total cell counts for measuring density.

Immunofluorescence slides were imaged with an AXIO Examiner D1 microscope (Zeiss) with confocal scanner unit (Yakagawa) using SlideBook software 6.0. All images in each experiment were captured using the same setting and batch normalize to make sure the signals in each channel were specific and under at the identical setting. Images were then analyzed by ImageJ (FIJI) agnostic to sample information. For each channel (DAPI, K8 and K14), the same threshold was applied to all images to identify region of interest and count numbers of positive cells. For measuring protein expression levels, IntegrateDensity of specific proteins in region of interest was measured and normalized to DAPI$^+$ area. Additional details of quantification for individual experiments were included in figure legends.

Tissue sections of 20 human DCIS cases were deparaffinized and quenched with 3% hydrogen peroxide (Sigma-Aldrich, 31642) in methanol, followed with antigen retrieval in antigen unmasking solution (Vector Laboratories, H-3300) for 15 min at 121 °C and blocking with 5% goat serum for 1 hr. For immunofluorescence, sections were stained with anti-SOX9-AF488 (1:100, Abcam, EPR14335), anti-B7x-AF647 (1:500, Abcam, EPR20236) and anti-E-Cadherin (1:300, BD Biosciences, BDB610182) followed with secondary antibody staining using anti-mouse IgG AF568 and DAPI. 3–5 representative images per case with DCIS histology were captured and batch renormalized as described above and imported to QuPath (v0.3.2) [73] for analysis. E-Cadherin$^+$ areas were used to generate annotation masks for DCIS. These annotated areas were segmented at single cell level based on DAPI using the same "positive cell detection" for all the images. For each DCIS cell, mean intensity of B7x and nuclear SOX9 were calculated. Total 41631 cells were measured for spearman correlation analysis. The mean intensity of each representative image was calculated by the sum of signal of each cell (intensity x cell area) normalized to the total cell area. Mean intensity of each case was calculated by the average of mean intensity of all the fields. CD8 IHC was performed on the consecutive sections. The same ducts used for SOX9 and B7x IF quantification were selected for CD8 quantification using ImageJ (FIJI). Epithelial CD8 density was calculated by the number of CD8$^+$ T cells within the epithelial region normalized to 10^5 μm^2 DCIS area. Correlation plots were generated with plot function or ggplot2 (v3.4.0) in R, a regression line was added using lm functions.

Multiplex imaging on tissue microarray—The breast cancer tissue microarray was purchased from US Biomax (BR1902) and submitted to the HIMSR at University of Colorado for multiplex imaging (mIF) and initial analysis. mIF was performed using 7-Color Opal Polaris reagent kit (Akoya Biosciences) following the manufactures' instructions with Leica Bond Rx Automated Stainer (Leica Biosystems), which was followed by whole slide scanning and Vectra Polaris multispectral imaging (Perkin Elmer). The panel used in this study is: anti-B7x (Cell Signaling Technology, 1:200, 14572S, Opal 570), anti-CD4 (Leica, PA0427, Opal 520), anti-p-STAT3 (Cell Signaling Technology, 1:300, 9145S, Opal 690), anti-SOX9 (Millipore, 1:1000, AB5535, Opal 620), anti-CD8 (Dako, 1:200, M7103, Opal 480), anti-pan-CK (Dako, 1:250, M3515, Opal 780), and DAPI. Slides were visualized with Phenochart (v1.1.0, Akoya Biosciences) to generate annotated images, which were further imported to inForm (v2.6.0, Akoya Biosciences) for cell segmentation and tissue segmentation (tumor/stroma) with the confirmation of a trained pathologist in a blinded view. The cell count, intensity, percentages, and H score analyses were generated using phenoptr (v0.3.2) and phenoptrReports (v0.3.3) R packages. Correlation plots for protein expression per case or at single cell level (Log_2(intensity+0.01)) were generated with plot function or ggplot2 (v3.4.0) in R, a regression line was added using lm functions.

Western blotting—The cells were lysed in RIPA buffer with protease and phosphatase inhibitors and centrifuged at 18000 g for 10 min at 4 °C. Protein lysates were separated with 4–12% NuPAGE Bis-Tris Protein Gels (Invitrogen) and wet tank transferred to a PVDF membrane (Millipore). The membrane was blocked with 5% non-fat dry milk in PBST and then incubated with primary antibodies against SOX9 (1:1000, Cell Signaling Technology, 82630S), B7x (1:1000, Cell Signaling Technology, 14572S), STAT3 (1:1000, Cell Signaling Technology, 9139S), p-STAT3 (1:1000, Cell Signaling Technology, 9145S), p-JAK1 (1:1000, Cell Signaling Technology, 3331S), p-JAK2 (1:1000, Cell Signaling Technology, 3776S), β-actin (1:5000, BD Biosciences, 612656), or Histone H3 (1:10000, Cell Signaling Technology, 14269S). The membrane was incubated with Western Lightning ECL Pro (PerkinElmer) and imaged using films or the Odyssey® Fc (Li-Cor).

ELISA—MCF7ras Ctrl and tetO-SOX9 cells were pre-treated with 2 μg/ml doxycycline for 96 hours. The culture supernatants were collected and centrifuged at 1000 g for 10 min at 4 °C to remove debris. The whole cell protein from the same well were isolated and lysed in RIPA buffer with protease and phosphatase inhibitors. The total amount of the whole cell protein was measured by DC Protein Assay kit (Bio-Rad, 500–0116) and used for normalization. The culture supernatants were subjected to ELISA with Human LIF ELISA Kit (Invitrogen, BMS242) following the manufacturers' instructions.

qRT-PCR—Total RNA was isolated from the cells using Direct-zol RNA Miniprep Plus kit (Zymo Research). cDNA was synthesized from total RNA with the High-Capacity cDNA Reverse Transcription Kit (Applied Biosystems). Real-time PCR was performed with SYBR Green PCR Master Mix (Applied Biosystems) in the QuantStudio 6 Flex Real-Time PCR System (Applied Biosystems). Primers are listed in Table S1.

Mammary epithelial cell and tumor cell isolation—Mammary epithelial cells were prepared as described [18]. Mammary tumors were dissected, minced, and digested in DMEM/F12 medium (Corning, 10-092-CV) with 300 units/ml Collagenase 3 (Worthington, LS004182), 10 units/ml DNase I (Worthington, LS002139), and hyaluronidase (Worthington, LS002592) with rotating for 2 hours at 37 °C. After washing with cold PBS, RBCs were removed by RBC lysis buffer (eBioscience, 00-4300-54). Cells were then further dissociated with 0.05% Trypsin-EDTA and then with 1 U/ml Dispase (Worthington LS02109) and 100 U/ml DNase I (Worthington LS002139). Final suspensions were passed through a 40 μm filter.

Flow cytometry and cell sorting—Single cell suspensions were stained with primary antibodies at 1:100 dilution in staining buffer (PBS with 2% FBS and 2 mM EDTA) unless specified otherwise. The following antibodies were used: anti-mouse

B7x-APC or -PE (HMH4–5G1, BioLegend), anti-human B7x-APC or -PE (MIH43, BioLegend), anti-human CD3-APC (SK7, BioLegend), anti-human HLA-A2-APC (BB7.2, BioLegend), anti-mouse CD45-Pacific Blue (30-F11, BioLegend), anti-mouse CD3-APC (17A2, BioLegend), anti-mouse CD4-APC/Cy7 (GK1.5, BioLegend), anti-mouse CD8a-PE (53–6.7, BioLegend), anti-mouse B7-H3-PE (MIH35, BioLegend), anti-mouse PD-L1-PE (10F.9G2, BioLegend), anti-mouse Ter119-biotin (TER-119, BioLegend), anti-mouse CD31-biotin (390, BioLegend), anti-mouse CD45-biotin (30-F11, BioLegend), Streptavidin-V450 (cat#560797, BD Biosciences), anti-EpCam-APC or -PerCP/Cy5.5 (G8.8, eBioscience), anti-CD49f-PerCP/Cy5.5 (GoH3, BD Biosciences), anti-CD166-PE (eBioALC48, eBioscience), anti-CD117-PE/Cy7 (2B8, BD Biosciences), anti-Sca1-APC/Cy7 (D7, BioLegend), anti-CD49b-AF488 (HMα2, BioLegend). DAPI or Ghost Dye Red 780 (Tonbo) was used to remove dead cells.

To profile immune cell populations after anti-B7x treatment, tumors were digested into single cells and stained with viability marker (Ghost Dye Red 780 (Tonbo)) for 30 minutes and followed by a cocktail of Abs for myeloid cell panel or T cell panel surface markers for 30 minutes: anti-CD45-Pacific Blue (30-F11), anti-CD3-FITC or PE (17A2), anti-CD4-BUV496 (GK1.5), anti-CD8a-PE/Dazzle594 (53–6.7), anti-CD25-PerCP/Cy5.5 (PC61), anti-CD11b-BV510 (M1/70), anti-Ly6C-PE/Dazzle594 (HK1.4), anti-Ly6G-APC (1A8), anti-CD11c-FITC (N418), anti-F4/80-PE/Cy5 (BM8), all from BioLegend or BD Biosciences. Intracellular staining was performed with the eBioscience Transcription Factor Staining Buffer (Thermo fisher) for anti-FOXP3-PE/Cy5 (FJK-16s, eBioscience) for 1 hour. Anti-rat/hamster Ig or anti-mouse Ig CompBeads (BD Biosciences) were used for compensation. Cells were analyzed on LSRII equipped with FACS Diva 6.1 software (BD Biosciences) or sorted by MoFlow Astrios Cell Sorter (Beckman Coulter). Data analysis was performed using FlowJo 10.

For mammary gland immune cell profiling, lymph nodes were removed from #3 and #4 mammary glands of 4–5 months old *Sox9*-WT;C3-TAg and *Sox9*-cKO;C3-TAg mice. The tissue was minced and digested in DMEM/F12 medium with 300 units/ml Collagenase 3 (Worthington, LS004182) and 10 units/ml DNase I with rotating for 1.5 hours at 37 °C. After RBC lysis, cells were filtered and stained with extracellular and intracellular markers: CD45-FITC (30-F11), Ly6G-PerCP-eFluor710 (1A8), Ly6C-biotin (AL-21), Streptavidin-BUV395, CD11c-BUV496 (N418), F4/80-eFluor 506 (BM8), CD8a-BV711 (53–6.7), CD3-BV750 (17A2), NK1.1-BV785 (PK136), CD169-eFluor660 (SER-4), CD4-Alexa Fluro 700 (RM4–5), CD19-APC/Cy7 (6D5), CD11b-PE/Dazzle594 (M1/70), CD115-PE/Cy7 (AFS98). Cells were acquired on Aurora spectrum cytometer (Cytek) and analyzed using FlowJo 10.

SOX9-overexpression in primary basal and luminal cells—Basal cells (DAPI$^-$CD45$^-$CD31$^-$Ter119$^-$EpCam^{low}CD49^{high}) and luminal cells (DAPI$^-$CD45$^-$CD31$^-$Ter119$^-$EpCam^{high}CD49^{low}) were sorted from mammary epithelial cells isolated from adult FVB/NJ mice. Basal cells and luminal cells were then seeded in 2D culture in organoid culture medium without Matrigel for lentiviral transduction with pLVX-puro (Takara 632164) and SOX9 overexpressing vector (pLVX-puro cloned with mouse SOX9 CDS and stop codon). After puromycin selection for 6–8 days, cells were lysed for WB analysis.

Generation of monoclonal antibody against B7x—Mouse anti-hB7x monoclonal antibody clone H19 was generated by standard hybridoma techniques [74]. Briefly, splenocytes from hB7x-IgV-Ig immunized B7x$^{-/-}$ BALB/c mice were fused with NSO myeloma cells. Clones including H19 that recognized hB7x, but not other irrelevant protein presented on 3T3 cell surface, were selected by high throughput flow cytometry. Hybridoma cells were cultured in CELLine 350 Bioreactor Flask (DWK Life Sciences). The cell compartment media was DMEM (Hyclone) supplemented with 10% ultra-low IgG FBS (Thermo Fisher), 10% NCTC-109 (Thermo Fisher), 1% nonessential amino acids, 100 U/ml penicillin and 100 μg/ml streptomycin. The medium compartment media was DMEM (Hyclone) supplemented with 100 U/ml penicillin and 100 μg/ml streptomycin. Antibodies were purified from hybridoma supernatant by Protein G resin (GenScript) columns. The purity and identity of antibodies were confirmed by SDS-PAGE. Generation of anti-mB7x mAb 1H3 was previously reported [50].

Primary human T cell isolation—Human PBMCs from healthy donors were purchased from New York Blood Center and isolated using Lymphoprep (Stemcell Technologies). CD4$^+$ or CD8$^+$ T cells were purified from the PBMCs using iMag human CD4$^+$ or CD8$^+$ lymphocyte enrichment sets (BD Biosciences) and CD4 or CD8 magnetic beads (Miltenyi). Isolated CD8$^+$ T cells were cultured in CTS OpTmizer media (Gibco) supplemented with 1% L-glutamine, penicillin (100 U/ml), streptomycin (100 μg/ml), anti-CD3/CD28 Dynabeads (Gibco), and IL-2 (100 U/ml; BioLegend).

Generation of primary CD8$^+$ T cells expressing NY-ESO-1 TCR—NY-ESO-1 specific TCR alpha chain (Addgene #112022) and beta chain (Addgene #112021) [34] were cloned into pCDH-EF1-IRES-EGFP (Addgene #128059). A 24-well non-tissue culture treated plate was coated with 10 μg/ml retronectin for 2 hours at room temperature. The retronectin-coated wells were blocked with FBS and washed with PBS. Lentivirus generated from pCDH-EF1-TCRα/β-IRES-EGFP was added to the wells and centrifuge at 2000 g for 2 hours. The supernatant was then removed, and the wells were washed with PBS. Expanded CD8$^+$ T cells were added to the virus-coated plate and centrifuge at 1000 g for 10mins. After culture, NY-ESO-1 TCR$^+$ T cells were isolated by FACS and expanded in T cell culture medium with IL2.

***In vitro* cytotoxicity assays—**MCF7ras ctrl and tetO-SOX9 cells were pretreated with 2 μg/ml doxycycline for 72 hours and then co-cultured with NY-ESO-1 TCR$^+$ human CD8$^+$ T cells at effector (T cell) to target (tumor cells) (E:T) ratio = 2:1 for 72 hours in RPMI1640 medium with 10% FBS, 1% Penicillin/Streptomycin, 1% L-glutamine, 1% NEAA, 1% sodium pyruvate, 1:1000 β-mercaptoethanol and 2 μg/ml doxycycline. 20 μg/ml H19 anti-B7x or isotype control was added to coculture medium to assess the effect of B7x on cytotoxicity. Cytotoxicity was determined by flow cytometry.

Tumor cell – T cell coculture proliferation assay—MCF7ras or HCC1937 ctrl and tetO-SOX9 cells were pretreated with 2 μg/ml doxycycline for 72 hours. After harvested from culture, tumor cells were treated with 50 μg/ml mitomycin-c for 30 minutes at 37 °C. T cells were labeled with 1 μM CellTrace Violet (CTV, Invitrogen C34571) for 5 minutes. Tumor cells were then washed twice with medium, and co-cultured with T cells at a 1:2 ratio (50K tumor cells to 100K T cells) for 72 hours in RPMI1640 medium with 10% FBS, 10Mm HEPES, 1% L-glutamine, 1% NEAA, 1% sodium pyruvate, 1:1000 β-mercaptoethanol, 20K anti-CD3/CD28 Dynabeads, and 2 μg/ml doxycycline. Proliferation of $CD4^+$ and $CD8^+$ T cells was measured by CTV dye dilution using flow cytometry.

Depletion of T cells using anti-CD4/anti-CD8 antibodies—3-month-old MMTV-iCre;*Sox9*$^{Fl/Fl}$;C3-TAg mice and *Sox9*-GFP;C3-TAg mice received i.p injections with the cocktail of 200 μg αCD4 (Bio X Cell, BP0003–1) and 200 μg αCD8 (Bio X Cell, BE0223) or isotype controls (Bio X Cell, BP0090 and BE0088) every 5 days for 2 months. After 3 doses or at the endpoint of treatment, peripheral blood was collected by retro-orbital bleeding of mice and used for flow cytometry to determine depletion efficiency. Tumor onset was monitored by palpation every 5 days. Tissues were harvested for histology analysis at the endpoint of treatment or until mice had tumor onset (when tumor reached 3–4 mm in diameter).

B7x overexpression in *Sox9*-cKO;C3-TAg mammary epithelial organoids—Mouse B7x CDS with stop codon was cloned into pHIV-dTomato (Addgene #21374, a gift from Bryan Welm). Mammary epithelial cells were isolated from 6-month-old MMTV-iCre;*Sox9*$^{Fl/Fl}$;C3-TAg mice before tumor onset and transduced with pHIV-dTomato (ctrl) or pHIV-mB7x-dTomato (B7x-OE) in organoid culture. After FACS sorting, 2×10^5 $dTomato^+$ organoids were transplanted into #4 cleared mammary fat pads of 3-4-week-old REAR mice, and then tumor onset was monitored by weekly palpation. For histological analysis of MINs, 10^5 $dTomato^+$ organoid cells were transplanted in adult REAR mice through intraductal injections, and tissues were harvested for analysis two months after intraductal injection.

Treatment with anti-B7x and anti-PD-L1—1×10^6 primary tumor cells isolated from C3-TAg mice were orthotopically transplanted into #3 fat pads of 6–8 week-old C3-TAg REAR mice. 8×10^5 cells dissociated from *Pik3ca*^{H1047R}/*p53*^{null} organoids were orthotopically transplanted into #3 fat pads of 6–8 week-old FVB/NJ mice. *Pik3ca*^{H1047R}/*p53*^{null} organoids were generated as described previously [40]. After tumor onset, recipient mice were i.p. injected with 10 mg/kg anti-B7x (1H3) or mouse IgG1 isotype control (Bio X Cell, BE0083) every 3 days for four doses. Tumor volume was measured by caliper and calculated as V = (½) X (Length) X (Length) X (Width). On day 12, tumors were harvested for flow cytometry or histology analysis.

For spontaneous tumor model, after tumor onset, $B7x^{-/-}$;C3-TAg and $B7x^{+/+}$;C3-TAg mice received i.p. injections with 10 mg/kg αPD-L1 (Bio X Cell, BE0101) or isotype control (Bio X Cell, BE0090) every 3 days for four doses. Tumor volume was measured by caliper and calculated as V = (½) X (Length) X (Length) X (Width). Tumors were collected for histology analysis from 7 to 12 days after the last dose.

Mammary ductal tree regeneration by cleared fat pad transplantation—Mammary epithelial cells were isolated from 8-week-old BALB/c and $B7x^{-/-}$ mice and maintained in organoid culture for three passages. 2×10^5 cells dissociated from organoids were transplanted into #4 cleared mammary fat pads of 3-4-week-old BALB/c mice or Rag1$^{-/-}$ mice. 11 weeks after transplantation, #4 mammary glands were dissected out and stained for carmine staining using the protocols described previously [18].

Microarray and RNA-seq analysis—Microarray data of *Sox9*-WT and *Sox9*-cKO ER^{-} luminal cells, *Sox9*-GFP^{high} and *Sox9*-GFP^{low} luminal cells was published (GEO: GSE135892) and GSEA analysis was performed as described [18]. The list of immune checkpoint genes was adapted from previous studies [75,76]. The list of EMP genes was adapted from previous studies [23]. For RNA-seq, total RNA was isolated from MCF7ras ctrl and SOX9-OE cells using Direct-zol RNA Miniprep Plus kit and submitted to Novogene for library preparation and sequencing (Illumina NovaSeq 6000 PE150). RNA-seq reads were aligned using STAR (version 2.4.0) to the reference human genome (GRCh38.p13) with GENCODE annotation (gencode.v33). DESeq2 (v1.30.1) R package [77] was applied to analyze the differential expression at adjusted p-value < 0.05. Heatmaps were generated using pHeatmap (v1.0.12) R package. Upstream regulators were analyzed by IPA (QIAGEN). The gene list of STAT3 activators was adapted from previous study [49].

Single-cell RNA-seq analysis—Mammary epithelial cells were isolated from 3.5-month-old *Sox9*-GFP;C3-TAg mice and *Sox9*-GFP control mice and FACS sorted for live luminal cells (DAPI^{-}CD45^{-}CD31^{-}Ter119^{-} EpCam^{high}CD49^{low}). For each genotype, 10^4 live luminal cells with viability higher than 90% as determined by trypan blue staining were diluted to a final concentration around 1000 cells/μL and submitted to Einstein Genomics Core for scRNA-seq library construction. Single cell gel Bead-in-emulsions (GEMs) generation and barcoding, post GEM-RT cleanup and cDNA amplification, and library construction were performed using 10X Genomics Chromium Next GEM 3' v3.1 kit following the manufacturer’s instructions. HS DNA Bioanalyzer was used for cDNA quantification. The 10X single cell libraries were then submitted to Genewiz for sequencing (Illumina HiSeq 4000 PE150). 10X Genomics Cell Ranger (v3.1.0) was used for generating count matrices from demultiplexed scRNA-seq fastq files against the mm10 genome. At least 8993 cells were captured for each sample.

scRNA-seq data were processed and analyzed using Seurat (v3.2.2). Cells with either gene counts <200 or >6000 or a mitochondrial gene ratio of above 10% were filtered out and excluded for downstream analysis. Samples were integrated using the Seurat anchor-based integration method [78]. The first 20 principal components were used for computing the dimensional reduction using the UMAP method and clustering the cells. The resolution parameter was set as 0.5 in Seurat “FindClusters” function. ER^{-} luminal subset clusters that lacking Esr1 expression were defined and combined into 6 clusters (C1, C2, C3, C4, C5, and EMP which is unique in C3-TAg sample). pHeatmap (v1.0.12) R package was used to generate the heatmap for the genes of interest in each cluster based on Log_2(expression+0.01).

Published scRNA-seq count matrix and metadata of human TNBC patient samples was downloaded from GEO (GSE176078) and created as Seurat objects by Seurat (v4.1.1). Using the subtype and cell type annotation provided by the authors [52], cancer epithelial cells from TNBC subtype were extracted for further analyses. pHeatmap (v1.0.12) R package was used to generate the heatmap for the genes of interest in each cluster based on Log_2(expression+0.1). Spearman's correlation coefficent between genes were computed by the correlatePairs method in scran (v1.26.0) R package [79].

Chromatin Immunoprecipitation (ChIP)—Around 3×10^6 MCF7ras ctrl, MCF7ras SOX9-OE, and MDA-MB-468 cells were crosslinked with 1% PFA at room temperature for 10 minutes, quenched with 125 mM Glycine, and rinsed twice with 1X PBS. Cells were lysed and sonicated at 4 °C using a Bioruptor sonicator (Diagenode, UCD-200TM) into 100–600 bp fragments. The samples were incubated overnight at 4 °C with Dynabeads Protein A (Invitrogen, 10002D), which had been pre-coated with 5 μg anti-SOX9 (Millipore, AB5535) or Rabbit IgG (Cell Signaling Technology, 3900S). The ChIP samples were then washed, eluted, and reversed cross-linking by overnight incubation at 65 °C. Afterward, ChIP DNA was purified by phenol:chloroform:isoamyl alcohol (Sigma-Aldrich, 77677–100ML) and used for qPCR analysis. Primers used for ChIP-qPCR are listed in Table S1.

ChIP-seq and data analysis—Two replicates of SOX9 ChIP using anti-SOX9 (Millipore, AB5535) were performed in MCF7ras ctrl and MCF7ras SOX9-OE cells (with 5% spike-in mouse gDNA). The ChIP DNA samples were submitted to Genewiz for sequencing (Illumina HiSeq 4000 2×150 bp). ChIP-seq reads were aligned to the human genome (hg38) using bowtie2 (v2.4.2). BBTools seal.sh (v38.90, https://jgi.doe.gov/data-and-tools/bbtools/bb-tools-user-guide/seal-guide/) was used to separate human reads and spike-in mouse reads. Peaks were called by Genrich (v0.6.1) using MCF7ras ctrl SOX9 ChIP as controls and the option (-q 0.05). Deeptools (v3.5.0) bamCoverage was used to generate the bigwig file (bin size 10 and normalizing using RPGC) and used for generating heatmap. The enrichR (v3.0) R package was used to analyze the pathways enriched with SOX9-binding peaks. Motif analysis on peaks was performed with Homer (v4.11). MCF7 STAT3/p-STAT3 ChIP-seq data was published and downloaded from GEO (GSE126004) [48]. Overlapping of SOX9 and STAT3 or pSTAT3 peaks was analyzed using BEDTools (v2.30.0) intersect function. Integrative Genomics Viewer (IGV) was used to visualize ChIP-seq signal at specific loci.

TCGA data analysis—TCGA BRCA data was downloaded from UCSC Xena (https://xena.ucsc.edu/). For GSEA analysis, raw counts from TCGA BRCA tumor samples were processed using R package DESeq2 (v1.28.1), samples were ranked by expression level of *SOX9* or *VTCN1*. The top 25% and bottom 25% samples were used to run GSEA against the C2 KEGG gene set from MSigDB using fgsea (v1.14.0) [80]. TIMER 2.0 (http://timer.cistrome.org/) was used to estimate the correlation of the SOX9-STAT3-B7x axis with tumor-infiltrating immune cells in human TCGA BRCA patients.

QUANTIFICATION AND STATISTICAL ANALYSIS

Data are represented as mean ± SEM. Statistical tests were performed using GraphPad Prism V9.3.0 (San Diego, CA). Comparisons between two groups were performed using a two-tailed unpaired Student's t-test. One-way ANOVA with Dunnett or Tukey test was used when three or more groups were compared. For nonparametric data that were not normally distributed, Kruskal-Wallis with Dunn's test (comparisons among three or more groups) or

Mann Whitney U test (comparisons between two groups) was used. The differences between variables in a contingency table were analyzed by Fisher's exact test. For Kaplan-Meier survival curves, p values were calculated by the log-rank test. Primary tumor growth over time was analyzed using two-way ANOVA with multiple comparisons. For correlation analysis, Spearman's correlation coefficient and p value were calculated using Prism.

Supplementary Material

Refer to Web version on PubMed Central for supplementary material.

ACKNOWLEDGEMENTS

We thank the technical assistance from Flow Cytometry, Histopathology, Analytical Imaging, and Stem Cell Isolation core facilities of Albert Einstein College of Medicine, supported by Einstein Cancer Center Support Grant (P30 CA013330), the NYSTEM shared facility grant support (C029154), and P250 high-capacity slide scanner (1S10OD026852–01A1). We also thank the Human Immune Monitoring Shared Resource at University of Colorado for performing the multiplex imaging analysis. This work is supported by DOD BCRP grants BC171714 (W.G.) and BC190403/P1 (X.Z. and W.G.) and NIH grants 5R01CA212424 (W.G.) and 1P01CA257885 (W.G.). Y.L. was supported by the NYSTEM Training Grant (C34874GG). W.G. was a V Scholar of the V Foundation for Cancer Research and supported by the Mary Kay Foundation.

REFERENCES

1. Hodi FS, O'Day SJ, McDermott DF, Weber RW, Sosman JA, Haanen JB, Gonzalez R, Robert C, Schadendorf D, Hassel JC, et al. (2010). Improved survival with ipilimumab in patients with metastatic melanoma. N. Engl. J. Med 363, 711–723. [PubMed: 20525992]
2. Herbst RS, Baas P, Kim DW, Felip E, Pérez-Gracia JL, Han JY, Molina J, Kim JH, Arvis CD, Ahn MJ, et al. (2016). Pembrolizumab versus docetaxel for previously treated, PD-L1-positive, advanced non-small-cell lung cancer (KEYNOTE-010): a randomised controlled trial. Lancet 387, 1540–1550. [PubMed: 26712084]
3. Reck M, Rodríguez-Abreu D, Robinson AG, Hui R, Csőszi T, Fülöp A, Gottfried M, Peled N, Tafreshi A, Cuffe S, et al. (2016). Pembrolizumab versus Chemotherapy for PD-L1-Positive Non-Small-Cell Lung Cancer. N. Engl. J. Med 375, 1823–1833. [PubMed: 27718847]
4. Schmid P, Adams S, Rugo HS, Schneeweiss A, Barrios CH, Iwata H, Diéras V, Hegg R, Im SA, Shaw Wright G, et al. (2018). Atezolizumab and Nab-Paclitaxel in Advanced Triple-Negative Breast Cancer. N. Engl. J. Med 379, 2108–2121. [PubMed: 30345906]
5. Cortes J, Cescon DW, Rugo HS, Nowecki Z, Im SA, Yusof MM, Gallardo C, Lipatov O, Barrios CH, Holgado E, et al. (2020). Pembrolizumab plus chemotherapy versus placebo plus chemotherapy for previously untreated locally recurrent inoperable or metastatic triple-negative breast cancer (KEYNOTE-355): a randomised, placebo-controlled, double-blind, phase 3 clinical trial. Lancet 396, 1817–1828. [PubMed: 33278935]
6. Wein L, Luen SJ, Savas P, Salgado R, and Loi S (2018). Checkpoint blockade in the treatment of breast cancer: current status and future directions. Br. J. Cancer 119, 4–11. [PubMed: 29808015]
7. Murciano-Goroff YR, Warner AB, and Wolchok JD (2020). The future of cancer immunotherapy: microenvironment-targeting combinations. Cell Res 30, 507–519. [PubMed: 32467593]
8. Gruosso T, Gigoux M, Manem VSK, Bertos N, Zuo D, Perlitch I, Saleh SMI, Zhao H, Souleimanova M, Johnson RM, et al. (2019). Spatially distinct tumor immune microenvironments stratify triple-negative breast cancers. J. Clin. Invest 129, 1785–1800. [PubMed: 30753167]
9. Song X, Zhou Z, Li H, Xue Y, Lu X, Bahar I, Kepp O, Hung M-C, Kroemer G, and Wan Y (2020). Pharmacologic Suppression of B7-H4 Glycosylation Restores Antitumor Immunity in Immune-Cold Breast Cancers. Cancer Discov 10, 1872. [PubMed: 32938586]
10. Zang X, Loke P, Kim J, Murphy K, Waitz R, and Allison JP (2003). B7x: a widely expressed B7 family member that inhibits T cell activation. Proc. Natl. Acad. Sci. U S A 100, 10388–10392. [PubMed: 12920180]

11. Janakiram M, Shah UA, Liu W, Zhao A, Schoenberg MP, and Zang X (2017). The third group of the B7-CD28 immune checkpoint family: HHLA2, TMIGD2, B7x, and B7-H3. Immunol. Rev 276, 26–39. [PubMed: 28258693]
12. Jeon H, Ohaegbulam KC, Abadi YM, and Zang X (2013). B7x and myeloid-derived suppressor cells in the tumor microenvironment: A tale of two cities. Oncoimmunology 2, e24744. [PubMed: 24073367]
13. Burstein MD, Tsimelzon A, Poage GM, Covington KR, Contreras A, Fuqua SA, Savage MI, Osborne CK, Hilsenbeck SG, Chang JC, et al. (2015). Comprehensive genomic analysis identifies novel subtypes and targets of triple-negative breast cancer. Clin. Cancer Res 21, 1688–1698. [PubMed: 25208879]
14. Huang H, Li C, and Ren G (2017). Clinical significance of the B7-H4 as a novel prognostic marker in breast cancer. Gene 623, 24–28. 10.1016/j.gene.2017.04.003. [PubMed: 28412458]
15. Van Keymeulen A, Lee MY, Ousset M, Brohée S, Rorive S, Giraddi RR, Wuidart A, Bouvencourt G, Dubois C, Salmon I, et al. (2015). Reactivation of multipotency by oncogenic PIK3CA induces breast tumour heterogeneity. Nature 525, 119–123. [PubMed: 26266985]
16. Koren S, Reavie L, Couto JP, De Silva D, Stadler MB, Roloff T, Britschgi A, Eichlisberger T, Kohler H, Aina O, et al. (2015). PIK3CA(H1047R) induces multipotency and multi-lineage mammary tumours. Nature 525, 114–118. [PubMed: 26266975]
17. Dravis C, Chung CY, Lytle NK, Herrera-Valdez J, Luna G, Trejo CL, Reya T, and Wahl GM (2018). Epigenetic and Transcriptomic Profiling of Mammary Gland Development and Tumor Models Disclose Regulators of Cell State Plasticity. Cancer Cell 34, 466–482 e466. [PubMed: 30174241]
18. Christin JR, Wang C, Chung C-Y, Liu Y, Dravis C, Tang W, Oktay MH, Wahl GM, and Guo W (2020). Stem Cell Determinant SOX9 Promotes Lineage Plasticity and Progression in Basal-like Breast Cancer. Cell Rep 31, 107742. [PubMed: 32521267]
19. Wang H, Xiang D, Liu B, He A, Randle HJ, Zhang KX, Dongre A, Sachs N, Clark AP, Tao L, et al. (2019). Inadequate DNA Damage Repair Promotes Mammary Transdifferentiation, Leading to BRCA1 Breast Cancer. Cell 178, 135–151.e119. 10.1016/j.cell.2019.06.002. [PubMed: 31251913]
20. Rios AC, Capaldo BD, Vaillant F, Pal B, van Ineveld R, Dawson CA, Chen Y, Nolan E, Fu NY, Jackling FC, et al. (2019). Intraclonal Plasticity in Mammary Tumors Revealed through Large-Scale Single-Cell Resolution 3D Imaging. Cancer Cell 35, 953. 10.1016/j.ccell.2019.05.011. [PubMed: 31185217]
21. Spike BT, Engle DD, Lin JC, Cheung SK, La J, and Wahl GM (2012). A mammary stem cell population identified and characterized in late embryogenesis reveals similarities to human breast cancer. Cell Stem Cell 10, 183–197. S1934–5909(12)00002–1 [pii] 10.1016/j.stem.2011.12.018 [doi]. [PubMed: 22305568]
22. Dravis C, Spike BT, Harrell JC, Johns C, Trejo CL, Southard-Smith EM, Perou CM, and Wahl GM (2015). Sox10 Regulates Stem/Progenitor and Mesenchymal Cell States in Mammary Epithelial Cells. Cell Rep 12, 2035–2048. [PubMed: 26365194]
23. Wuidart A, Sifrim A, Fioramonti M, Matsumura S, Brisebarre A, Brown D, Centonze A, Dannau A, Dubois C, Van Keymeulen A, et al. (2018). Early lineage segregation of multipotent embryonic mammary gland progenitors. Nat. Cell Biol 20, 666–676. [PubMed: 29784918]
24. Li J, and Stanger BZ (2020). How Tumor Cell Dedifferentiation Drives Immune Evasion and Resistance to Immunotherapy. Cancer Res 80, 4037–4041. [PubMed: 32554552]
25. Gibbs ZA, and Whitehurst AW (2018). Emerging Contributions of Cancer/Testis Antigens to Neoplastic Behaviors. Trends Cancer 4, 701–712. 10.1016/j.trecan.2018.08.005. [PubMed: 30292353]
26. Gjerstorff MF, Andersen MH, and Ditzel HJ (2015). Oncogenic cancer/testis antigens: prime candidates for immunotherapy. Oncotarget 6, 15772–15787. 10.18632/oncotarget.4694. [PubMed: 26158218]
27. Guo W, Keckesova Z, Donaher JL, Shibue T, Tischler V, Reinhardt F, Itzkovitz S, Noske A, Zurrer-Hardi U, Bell G, et al. (2012). Slug and Sox9 cooperatively determine the mammary stem cell state. Cell 148, 1015–1028. S0092–8674(12)00165–1 [pii] 10.1016/j.cell.2012.02.008 [doi]. [PubMed: 22385965]

28. Jo A, Denduluri S, Zhang B, Wang Z, Yin L, Yan Z, Kang R, Shi LL, Mok J, Lee MJ, and Haydon RC (2014). The versatile functions of Sox9 in development, stem cells, and human diseases. Genes Dis 1, 149–161. [PubMed: 25685828]
29. Wang C, Christin JR, Oktay MH, and Guo W (2017). Lineage-Biased Stem Cells Maintain Estrogen-Receptor-Positive and -Negative Mouse Mammary Luminal Lineages. Cell Rep 18, 2825–2835. [PubMed: 28329676]
30. Ge Y, Gomez NC, Adam RC, Nikolova M, Yang H, Verma A, Lu CP, Polak L, Yuan S, Elemento O, and Fuchs E (2017). Stem Cell Lineage Infidelity Drives Wound Repair and Cancer. Cell 169, 636–650 e614. [PubMed: 28434617]
31. Kopp JL, von Figura G, Mayes E, Liu FF, Dubois CL, Morris J.P.t., Pan FC, Akiyama H, Wright CV, Jensen K, et al. (2012). Identification of Sox9-Dependent Acinar-to-Ductal Reprogramming as the Principal Mechanism for Initiation of Pancreatic Ductal Adenocarcinoma. Cancer Cell 22, 737–750. S1535–6108(12)00449–7 [pii] 10.1016/j.ccr.2012.10.025 [doi]. [PubMed: 23201164]
32. Green JE, Shibata M-A, Yoshidome K, Liu M. l., Jorcyk C, Anver MR, Wigginton J, Wiltrout R, Shibata E, Kaczmarczyk S, et al. (2000). The C3(1)/SV40 T-antigen transgenic mouse model of mammary cancer: ductal epithelial cell targeting with multistage progression to carcinoma. Oncogene 19, 1020. [PubMed: 10713685]
33. Pfefferle AD, Herschkowitz JI, Usary J, Harrell JC, Spike BT, Adams JR, Torres-Arzayus MI, Brown M, Egan SE, Wahl GM, et al. (2013). Transcriptomic classification of genetically engineered mouse models of breast cancer identifies human subtype counterparts. Genome Biol 14, R125. [PubMed: 24220145]
34. Roth TL, Puig-Saus C, Yu R, Shifrut E, Carnevale J, Li PJ, Hiatt J, Saco J, Krystofinski P, Li H, et al. (2018). Reprogramming human T cell function and specificity with non-viral genome targeting. Nature 559, 405–409. [PubMed: 29995861]
35. Lim E, Vaillant F, Wu D, Forrest NC, Pal B, Hart AH, Asselin-Labat ML, Gyorki DE, Ward T, Partanen A, et al. (2009). Aberrant luminal progenitors as the candidate target population for basal tumor development in BRCA1 mutation carriers. Nat. Med 15, 907–913. [PubMed: 19648928]
36. Molyneux G, Geyer FC, Magnay FA, McCarthy A, Kendrick H, Natrajan R, Mackay A, Grigoriadis A, Tutt A, Ashworth A, et al. (2010). BRCA1 basal-like breast cancers originate from luminal epithelial progenitors and not from basal stem cells. Cell Stem Cell 7, 403–417. S1934–5909(10)00346–2 [pii] 10.1016/j.stem.2010.07.010 [doi]. [PubMed: 20804975]
37. Wei J, Loke P.n., Zang X, and Allison JP (2011). Tissue-specific expression of B7x protects from CD4 T cell-mediated autoimmunity. J. Exp. Med 208, 1683–1694. [PubMed: 21727190]
38. Abadi YM, Jeon H, Ohaegbulam KC, Scandiuzzi L, Ghosh K, Hofmeyer KA, Lee JS, Ray A, Gravekamp C, and Zang X (2013). Host B7x Promotes Pulmonary Metastasis of Breast Cancer. J. Immunol 190, 3806. [PubMed: 23455497]
39. Aprelikova O, Tomlinson CC, Hoenerhoff M, Hixon JA, Durum SK, Qiu TH, He S, Burkett S, Liu ZY, Swanson SM, and Green JE (2016). Development and Preclinical Application of an Immunocompetent Transplant Model of Basal Breast Cancer with Lung, Liver and Brain Metastases. PLoS One 11, e0155262. 10.1371/journal.pone.0155262. [PubMed: 27171183]
40. Cui J, Zhang C, Lee JE, Bartholdy BA, Yang D, Liu Y, Erler P, Galbo PM Jr., Hodge DQ, Huangfu D, et al. (2023). MLL3 loss drives metastasis by promoting a hybrid epithelial-mesenchymal transition state. Nat Cell Biol 25, 145–158. 10.1038/s41556-022-01045-0. [PubMed: 36604594]
41. Centonze A, Lin S, Tika E, Sifrim A, Fioramonti M, Malfait M, Song Y, Wuidart A, Van Herck J, Dannau A, et al. (2020). Heterotypic cell-cell communication regulates glandular stem cell multipotency. Nature 584, 608–613. 10.1038/s41586-020-2632-y. [PubMed: 32848220]
42. Rajagopal J, and Stanger BZ (2016). Plasticity in the Adult: How Should the Waddington Diagram Be Applied to Regenerating Tissues? Dev. Cell 36, 133–137. [PubMed: 26812013]
43. Yao Y, Ye H, Qi Z, Mo L, Yue Q, Baral A, Hoon DSB, Vera JC, Heiss JD, Chen CC, et al. (2016). B7-H4(B7x)-Mediated Cross-talk between Glioma-Initiating Cells and Macrophages via the IL6/JAK/STAT3 Pathway Lead to Poor Prognosis in Glioma Patients. Clin. Cancer Res 22, 2778–2790. [PubMed: 27001312]
44. Schust J, Sperl B, Hollis A, Mayer TU, and Berg T (2006). Stattic: a small-molecule inhibitor of STAT3 activation and dimerization. Chem. Biol 13, 1235–1242. [PubMed: 17114005]

45. Kuleshov MV, Jones MR, Rouillard AD, Fernandez NF, Duan Q, Wang Z, Koplev S, Jenkins SL, Jagodnik KM, Lachmann A, et al. (2016). Enrichr: a comprehensive gene set enrichment analysis web server 2016 update. Nucleic Acids Res 44, W90–97. [PubMed: 27141961]
46. Lachmann A, Xu H, Krishnan J, Berger SI, Mazloom AR, and Ma'ayan A (2010). ChEA: transcription factor regulation inferred from integrating genome-wide ChIP-X experiments. Bioinformatics 26, 2438–2444. [PubMed: 20709693]
47. Heinz S, Benner C, Spann N, Bertolino E, Lin YC, Laslo P, Cheng JX, Murre C, Singh H, and Glass CK (2010). Simple combinations of lineage-determining transcription factors prime cis-regulatory elements required for macrophage and B cell identities. Mol. Cell 38, 576–589. [PubMed: 20513432]
48. Siersbæk R, Scabia V, Nagarajan S, Chernukhin I, Papachristou EK, Broome R, Johnston SJ, Joosten SEP, Green AR, Kumar S, et al. (2020). IL6/STAT3 Signaling Hijacks Estrogen Receptor α Enhancers to Drive Breast Cancer Metastasis. Cancer Cell 38, 412–423.e419. [PubMed: 32679107]
49. Garbers C, Hermanns HM, Schaper F, Müller-Newen G, Grötzinger J, Rose-John S, and Scheller J (2012). Plasticity and cross-talk of interleukin 6-type cytokines. Cytokine Growth Factor Rev 23, 85–97. [PubMed: 22595692]
50. Jeon H, Vigdorovich V, Garrett-Thomson SC, Janakiram M, Ramagopal UA, Abadi YM, Lee JS, Scandiuzzi L, Ohaegbulam KC, Chinai JM, et al. (2014). Structure and cancer immunotherapy of the B7 family member B7x. Cell Rep 9, 1089–1098. [PubMed: 25437562]
51. Mosely SI, Prime JE, Sainson RC, Koopmann JO, Wang DY, Greenawalt DM, Ahdesmaki MJ, Leyland R, Mullins S, Pacelli L, et al. (2017). Rational Selection of Syngeneic Preclinical Tumor Models for Immunotherapeutic Drug Discovery. Cancer Immunol Res 5, 29–41. 10.1158/2326-6066.Cir-16-0114. [PubMed: 27923825]
52. Wu SZ, Al-Eryani G, Roden DL, Junankar S, Harvey K, Andersson A, Thennavan A, Wang C, Torpy JR, Bartonicek N, et al. (2021). A single-cell and spatially resolved atlas of human breast cancers. Nat Genet 53, 1334–1347. 10.1038/s41588-021-00911-1. [PubMed: 34493872]
53. Li T, Fu J, Zeng Z, Cohen D, Li J, Chen Q, Li B, and Liu XS (2020). TIMER2.0 for analysis of tumor-infiltrating immune cells. Nucleic Acids Res 48, W509–w514. [PubMed: 32442275]
54. Sharma P, and Allison JP (2015). Immune checkpoint targeting in cancer therapy: toward combination strategies with curative potential. Cell 161, 205–214. 10.1016/j.cell.2015.03.030. [PubMed: 25860605]
55. Hein SM, Haricharan S, Johnston AN, Toneff MJ, Reddy JP, Dong J, Bu W, and Li Y (2016). Luminal epithelial cells within the mammary gland can produce basal cells upon oncogenic stress. Oncogene 35, 1461–1467. 10.1038/onc.2015.206. [PubMed: 26096929]
56. Saghafinia S, Homicsko K, Di Domenico A, Wullschleger S, Perren A, Marinoni I, Ciriello G, Michael IP, and Hanahan D (2021). Cancer Cells Retrace a Stepwise Differentiation Program during Malignant Progression. Cancer Discov 11, 2638–2657. [PubMed: 33910926]
57. Yuan S, Norgard RJ, and Stanger BZ (2019). Cellular Plasticity in Cancer. Cancer Discov 9, 837–851. [PubMed: 30992279]
58. Ge Y, and Fuchs E (2018). Stretching the limits: from homeostasis to stem cell plasticity in wound healing and cancer. Nat. Rev. Genet 19, 311–325. [PubMed: 29479084]
59. Liu Y, and Guo W (2021). SOX factors as cell-state regulators in the mammary gland and breast cancer. Semin. Cell Dev. Biol 114, 126–133. [PubMed: 33583737]
60. Mehta GA, Khanna P, and Gatza ML (2019). Emerging Role of SOX Proteins in Breast Cancer Development and Maintenance. J. Mammary Gland Biol. Neoplasia 24, 213–230. [PubMed: 31069617]
61. Gil Del Alcazar CR, Huh SJ, Ekram MB, Trinh A, Liu LL, Beca F, Zi X, Kwak M, Bergholtz H, Su Y, et al. (2017). Immune Escape in Breast Cancer During In Situ to Invasive Carcinoma Transition. Cancer Discov 7, 1098–1115. [PubMed: 28652380]
62. Trinh A, Gil Del Alcazar CR, Shukla SA, Chin K, Chang YH, Thibault G, Eng J, Jovanović B, Aldaz CM, Park SY, et al. (2021). Genomic Alterations during the In Situ to Invasive Ductal Breast Carcinoma Transition Shaped by the Immune System. Mol Cancer Res 19, 623–635. 10.1158/1541-7786.Mcr-20-0949. [PubMed: 33443130]

63. Malladi S, Macalinao DG, Jin X, He L, Basnet H, Zou Y, de Stanchina E, and Massague J (2016). Metastatic Latency and Immune Evasion through Autocrine Inhibition of WNT. Cell 165, 45–60. 10.1016/j.cell.2016.02.025. [PubMed: 27015306]

64. Laughney AM, Hu J, Campbell NR, Bakhoum SF, Setty M, Lavallee VP, Xie Y, Masilionis I, Carr AJ, Kottapalli S, et al. (2020). Regenerative lineages and immune-mediated pruning in lung cancer metastasis. Nat Med 26, 259–269. 10.1038/s41591-019-0750-6. [PubMed: 32042191]

65. John P, Wei Y, Liu W, Du M, Guan F, and Zang X (2019). The B7x Immune Checkpoint Pathway: From Discovery to Clinical Trial. Trends Pharmacol. Sci 40, 883–896. [PubMed: 31677920]

66. Yu H, Pardoll D, and Jove R (2009). STATs in cancer inflammation and immunity: a leading role for STAT3. Nature reviews. Cancer 9, 798–809. [PubMed: 19851315]

67. Yu H, Lee H, Herrmann A, Buettner R, and Jove R (2014). Revisiting STAT3 signalling in cancer: new and unexpected biological functions. Nature reviews. Cancer 14, 736–746.

68. Jones LM, Broz ML, Ranger JJ, Ozcelik J, Ahn R, Zuo D, Ursini-Siegel J, Hallett MT, Krummel M, and Muller WJ (2016). STAT3 Establishes an Immunosuppressive Microenvironment during the Early Stages of Breast Carcinogenesis to Promote Tumor Growth and Metastasis. Cancer Res 76, 1416–1428. [PubMed: 26719528]

69. Zhang Z, Christin JR, Wang C, Ge K, Oktay MH, and Guo W (2016). Mammary-Stem-Cell-Based Somatic Mouse Models Reveal Breast Cancer Drivers Causing Cell Fate Dysregulation. Cell Rep 16, 3146–3156. [PubMed: 27653681]

70. Cui J, and Guo W (2021). Establishment and long-term culture of mouse mammary stem cell organoids and breast tumor organoids. STAR Protoc 2, 100577. [PubMed: 34124696]

71. Labun K, Montague TG, Krause M, Torres Cleuren YN, Tjeldnes H, and Valen E (2019). CHOPCHOP v3: expanding the CRISPR web toolbox beyond genome editing. Nucleic Acids Res 47, W171–W174. [PubMed: 31106371]

72. Schindelin J, Arganda-Carreras I, Frise E, Kaynig V, Longair M, Pietzsch T, Preibisch S, Rueden C, Saalfeld S, Schmid B, et al. (2012). Fiji: an open-source platform for biological-image analysis. Nature Methods 9, 676–682. 10.1038/nmeth.2019. [PubMed: 22743772]

73. Bankhead P, Loughrey MB, Fernández JA, Dombrowski Y, McArt DG, Dunne PD, McQuaid S, Gray RT, Murray LJ, Coleman HG, et al. (2017). QuPath: Open source software for digital pathology image analysis. Scientific Reports 7, 16878. 10.1038/s41598-017-17204-5. [PubMed: 29203879]

74. Zhao R, Chinai JM, Buhl S, Scandiuzzi L, Ray A, Jeon H, Ohaegbulam KC, Ghosh K, Zhao A, Scharff MD, and Zang X (2013). HHLA2 is a member of the B7 family and inhibits human CD4 and CD8 T-cell function. Proc. Natl. Acad. Sci. U S A 110, 9879–9884. [PubMed: 23716685]

75. Pardoll DM (2012). The blockade of immune checkpoints in cancer immunotherapy. Nature reviews. Cancer 12, 252–264. [PubMed: 22437870]

76. Wykes MN, and Lewin SR (2018). Immune checkpoint blockade in infectious diseases. Nat. Rev. Immunol 18, 91–104. [PubMed: 28990586]

77. Love MI, Huber W, and Anders S (2014). Moderated estimation of fold change and dispersion for RNA-seq data with DESeq2. Genome Biology 15, 550. 10.1186/s13059-014-0550-8. [PubMed: 25516281]

78. Stuart T, Butler A, Hoffman P, Hafemeister C, Papalexi E, Mauck WM 3rd, Hao Y, Stoeckius M, Smibert P, and Satija R (2019). Comprehensive Integration of Single-Cell Data. Cell 177, 1888–1902.e1821. 10.1016/j.cell.2019.05.031. [PubMed: 31178118]

79. Lun A, McCarthy D, and Marioni J (2016). A step-by-step workflow for low-level analysis of single-cell RNA-seq data with Bioconductor [version 2; peer review: 3 approved, 2 approved with reservations]. F1000Research 5. 10.12688/f1000research.9501.2.

80. Sergushichev AA (2016). An algorithm for fast preranked gene set enrichment analysis using cumulative statistic calculation. bioRxiv, 060012; doi: 10.1101/060012.

HIGHLIGHTS

- SOX9 suppresses T cell infiltration in DCIS to promote malignant progression.
- SOX9 upregulates B7x expression via STAT3 activation and direct binding to *VTCN1*.
- SOX9-B7x axis promotes immune escape of dedifferentiated tumor cells.
- B7x targeting inhibits BLBC tumor growth and confers a response to anti-PD-L1.

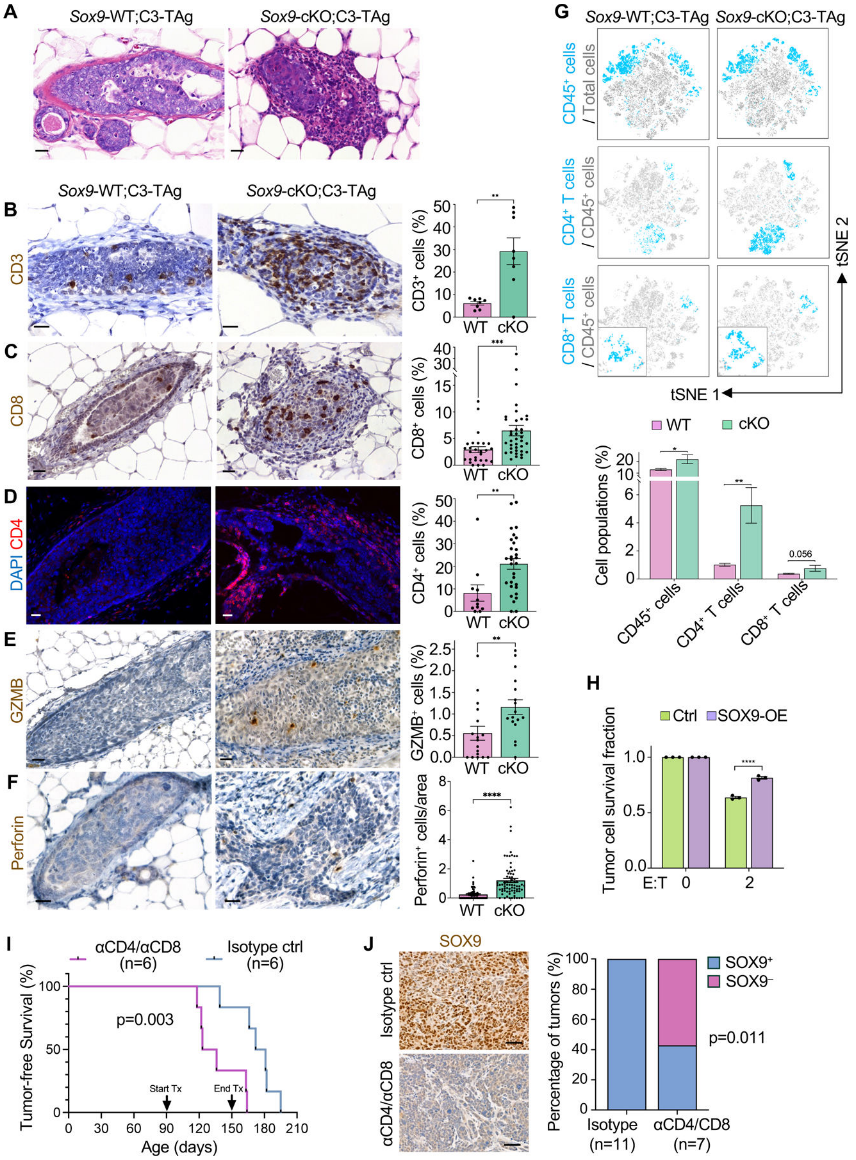

Figure 1. *Sox9* knockout leads to massive accumulation of infiltrating T cells inhibiting MIN progression.

(A) H&E staining of MIN lesions from *Sox9*-WT or *Sox9*-cKO;C3-TAg mice. Scale bars, 20 μm.

(B) Representative images of CD3 immunohistochemistry (IHC) and percentage of CD3$^+$ T cells among total cells in MINs. 8 MINs were analyzed in each group. Scale bars, 20 μm.

(C) Representative images of CD8 IHC and percentage of CD8$^+$ T cells among total cells in MINs. 27 MINs from 4 *Sox9*-WT;C3-TAg and 38 MINs from 4 *Sox9*-cKO;C3-TAg mice were analyzed. Scale bars, 20 μm.

(D) Representative images of CD4 immunostaining and percentage of CD4$^+$ T cells among DAPI$^+$ cells in MINs. 11 MINs from 3 *Sox9*-WT;C3-TAg and 33 MINs from 4 *Sox9*-cKO;C3-TAg mice were analyzed. Scale bars, 20 μm.

(E) Representative images of granzyme B (GZMB) IHC and percentage of GZMB$^+$ cells among total cells in MINs. 17 MINs from 4 mice in each group were analyzed. Scale bars, 20 μm.

(F) Representative images of perforin IHC and number of perforin$^+$ cells in each 10,000 μm^2 lesion area. >70 MINs from 6 mice in each group were analyzed. Scale bars, 20 μm.

(G) Spectral flow cytometry profiling immune cells in the indicated C3-TAg mammary glands. (left) The t-SNE (t-Distributed Stochastic Neighbor Embedding) plots were generated using flow cytometric data gated on total single cells or CD45$^+$ cells (n = 5 mice/group). The insets show zoom-in views of CD8$^+$ T cell clusters. (right) Percentage of immune cell populations normalized to total single cells (WT, n = 7 mice; cKO, n=5 mice).

(H) T cell cytotoxicity assay with MCF7ras Ctrl and SOX9-OE cells. Data represent the mean of three independent experiments using T cells from different donors. E:T indicates the ratio of effector (T cells) to target (tumor cells).

(I) Kaplan-Meier survival analysis of tumor onset in *Sox9*-cKO;C3-TAg mice treated with isotype ctrl or αCD4/αCD8 (n = 6 mice/group).

(J) Representative images of SOX9 IHC in tumors and percentages of SOX9$^-$ or SOX9$^+$ invasive tumors in mice treated as in (I) (isotype ctrl, 11 tumors; αCD4/αCD8, 7 tumors). Scale bars, 50 μm.

Data are summarized as mean ± SEM. An unpaired Student's t-test (B and G), Mann Whitney test (C-F), one-way ANOVA with Tukey's multiple comparisons test (H), log-rank test (I), or Fisher's exact test (J) was used to determine statistical significance. ****$p < 0.0001$; ***$p < 0.001$; **$p < 0.01$; *$p < 0.05$. See also Figures S1 and S2.

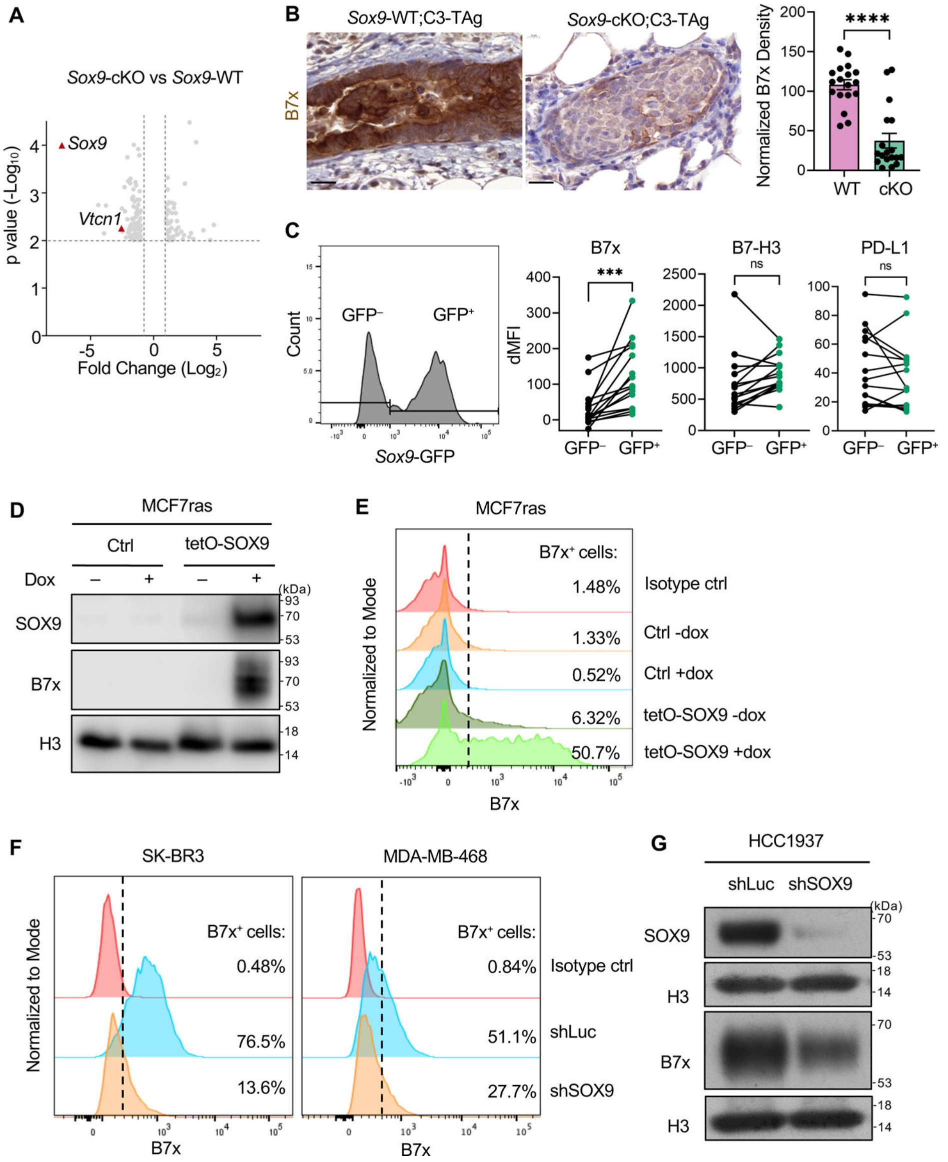

Figure 2. SOX9 upregulates immune checkpoint molecule B7x.

(A) Volcano plot showing differentially expressed genes (grey) between *Sox9*-WT and *Sox9*-cKO ER⁻ luminal cells, as determined by microarray ($p < 0.01$ and fold change ≥ 2).

(B) Representative images of B7x IHC and quantification of B7x intensity in MINs (n = 18 MINs from 4 mice/group). Mann Whitney test was used to determine statistical significance. Scale bars, 10 μm.

(C) Flow cytometry measuring B7x, B7-H3, and PD-L1 expression in *Sox9*-GFP$^+$ and *Sox9*-GFP$^-$ cells in C3-TAg invasive tumors (n = 15 tumors). Statistical significance was determined by paired Student's t-test.

(D) Western blot of SOX9 and B7x in MCF7ras Ctrl and tetO-SOX9 cells treated with doxycycline (dox) for 3 days.

(E) Flow cytometry measuring cell-surface B7x expression in MCF7ras Ctrl and tetO-SOX9 cells treated with dox for 6 days.

(F) Flow cytometry measuring cell-surface B7x expression in SK-BR3 and MDA-MB-468 shLuc and shSOX9 cells.

(G) Western blot of SOX9 and B7x in HCC1937 shLuc and shSOX9 cells.

Data are summarized as mean ± SEM. ****$p < 0.0001$; ***$p < 0.001$; n.s., not significant.

See also Figure S3.

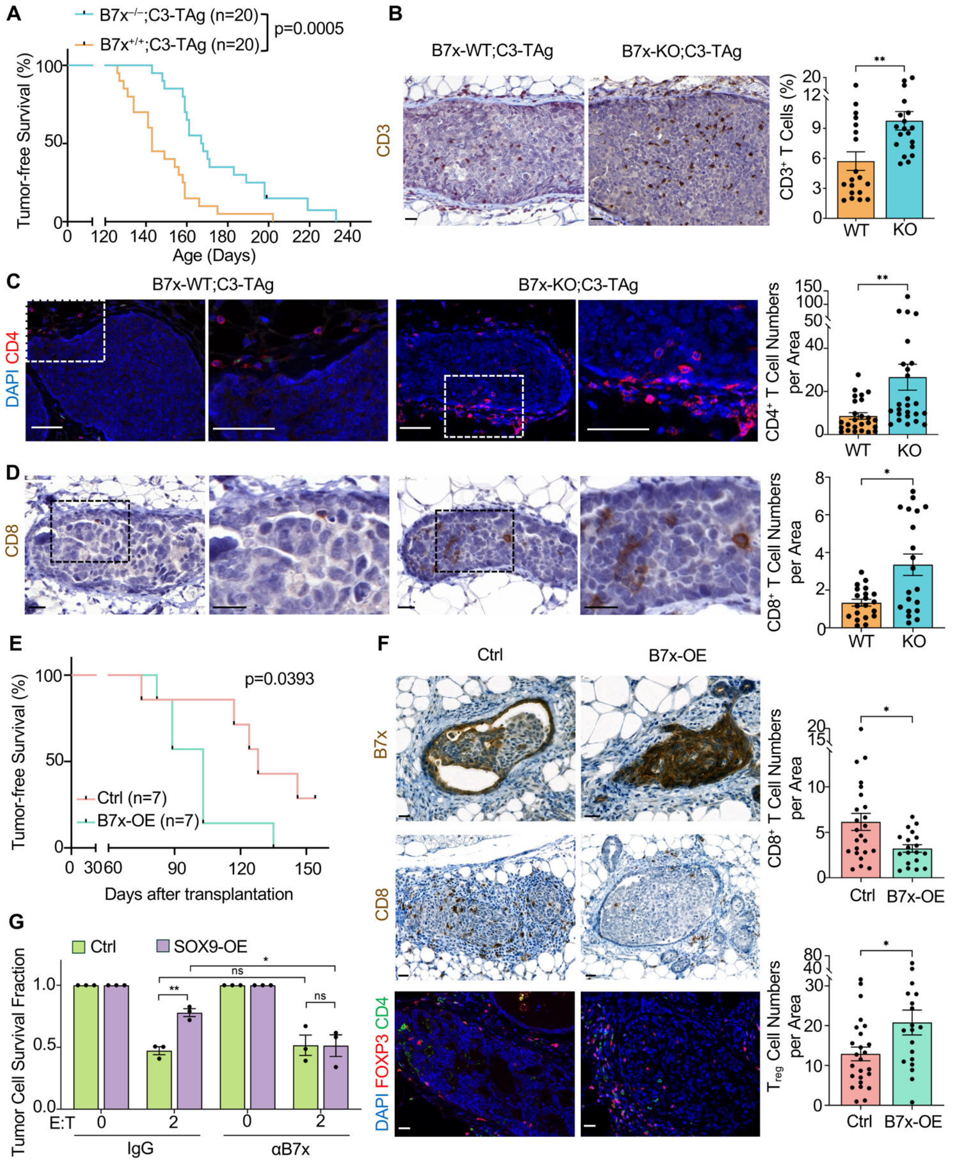

Figure 3. B7x acts downstream of SOX9 to suppress infiltrating T cells and promote tumor onset.

(A) Kaplan-Meier survival analysis of tumor onset in B7x-WT or B7x-KO;C3-TAg mice.

(B) Representative images of CD3 IHC and percentage of CD3$^+$ T cells among total cells in MINs. 19 MINs from 5 mice per group were analyzed. An unpaired Student's t-test was used to determine statistical significance. Scale bars, 20 μm.

(C) Representative images of CD4 immunostaining and CD4$^+$ T cell numbers per 10,000 μm^2 MIN area. 25 MINs from 5 mice per group were analyzed. Mann Whitney U test was used to determine statistical significance. Scale bars, 50 μm.

(D) Representative images of CD8 IHC and CD8$^+$ T cell numbers per 10,000 μm^2 MIN area. 20 MINs from 5 mice per group were analyzed. Mann Whitney U test was used to determine statistical significance. Scale bars, 20 μm.

(E) Kaplan-Meier survival analysis of tumor onset in mice transplanted with ctrl or B7x-OE *Sox9*-cKO;C3-TAg organoids in cleared mammary fat pads.

(F) Representative images of B7x, CD8, CD4 and FOXP3 immunostaining and quantification of $CD8^+$ T and $CD4^+FOXP3^+$ T_{reg} cell numbers per 10,000 μm^2 MIN area. 25 ctrl MINs from 7 transplants and 19 B7x-OE MINs from 4 transplants were analyzed. An unpaired Student's t-test was used to determine statistical significance. Scale bars, 20 μm.

(G) T cell cytotoxicity assay on MCF7ras Ctrl and SOX9-OE cells treated with αB7x or IgG. Data represent the mean of three independent experiments using T cells from different donors. Data were normalized to condition without T cells (Effector (E) : Target (T) = 0). One-way ANOVA with Tukey's multiple comparisons test was used to determine statistical significance.

Data are summarized as mean ± SEM. $^{**}p < 0.01$; $^{*}p < 0.05$; n.s., not significant. See also Figure S4.

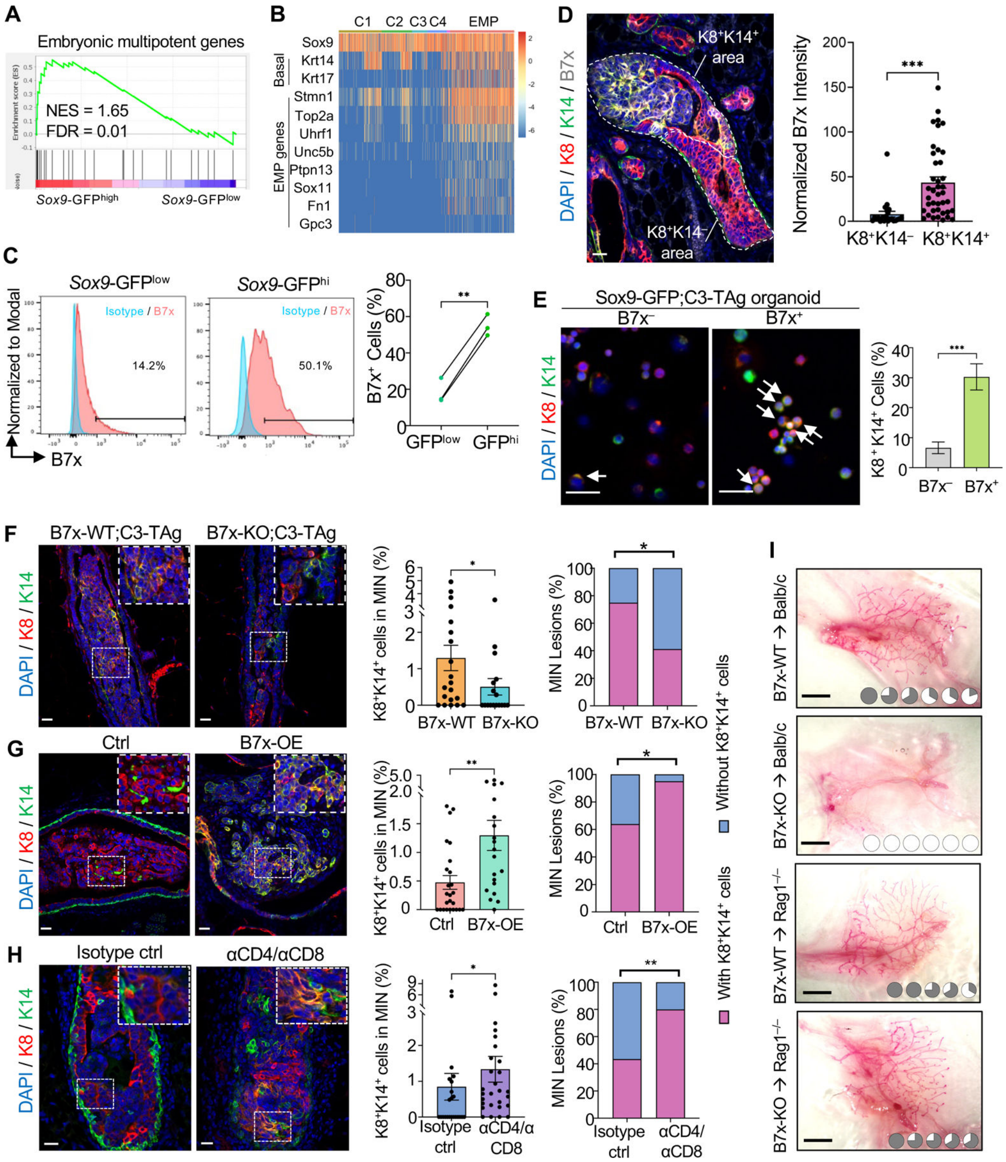

Figure 4. Dedifferentiated tumor cells require the SOX9-B7x axis to evade immunosurveillance.

(A) Gene set enrichment analysis (GSEA) comparing the embryonic multipotent progenitor (EMP) signature between *Sox9*-GFP^{high} and *Sox9*-GFP^{low} ER^{-} luminal cells in C3-TAg mice.

(B) Heatmap showing the basal and EMP gene expression in individual cells of ER^{-} luminal clusters as determined by single-cell RNA-seq (color scale, Log$_2$(expression+0.01)).

(C) Flow cytometry measuring cell-surface B7x expression in *Sox9*-GFP^{high} and *Sox9*-GFP^{low} ER^{-} luminal cells of 3-month-old *Sox9*-GFP;C3-TAg mice (n = 3 mice). A paired Student's t-test was used to determine statistical significance.

(D) Representative images of B7x, K8 and K14 immunostaining in MINs of 3-4-month-old *Sox9*-GFP;C3-TAg mice and B7x intensity normalized to total DAPI^{+} area within K8^{+}K14^{-} or K8^{+}K14^{+} MIN area. 23 K8^{+}K14^{-} areas and 40 K8^{+}K14^{+} areas from three C3-TAg mice were randomly selected for analysis. An unpaired Student's t-test was used to determine statistical significance. Scale bars, 20 µm.

(E) Representative images of K8 and K14 immunostaining in FACS-sorted B7x^{+} or B7x^{-} *Sox9*-GFP;C3-TAg mammary organoid cells and percentage of K8^{+}K14^{+} cells (arrows) in each population (B7x^{+}, n=9 fields; B7x^{-}, n=8 fields). An unpaired Student's t-test was used to determine statistical significance. Scale bars, 50 µm.

(F-H) Representative images of K8 and K14 immunostaining in MINs (left), percentage of K8^{+}K14^{+} cells in individual MINs (middle, statistical significance by Mann Whitney U test) and percentage of MINs with or without K8^{+}K14^{+} cells (right, statistical significance by Fisher's exact test). (F) 17 MINs from 3 B7x-KO;C3-TAg mice and 20 MINs from 3 B7x-WT;C3-TAg mice, (G) 25 ctrl MINs from 7 transplants and 20 B7x-OE MINs from 4 transplants, and (H) 28 MINs from 4 *Sox9*-cKO;C3-TAg mice treated with αCD4/αCD8 and 23 MINs from 5 *Sox9*-cKO;C3-TAg mice treated with isotype ctrls were randomly selected for imaging and analysis. All scale bars, 20 µm.

(I) Carmine staining of BALB/c or Rag1$^{-/-}$ cleared mammary fat pads transplanted with B7x-WT or B7x-KO mammary organoids. The grey area of each circle represents the extent of ductal tree outgrowth in each fat pad (BALB/c: n = 6/group; Rag1$^{-/-}$: n = 5/group). Scale bars, 2mm.

Data are summarized as mean ± SEM. $^{***}p < 0.001$; $^{**}p < 0.01$; $^{*}p < 0.05$. See also Figure S5.

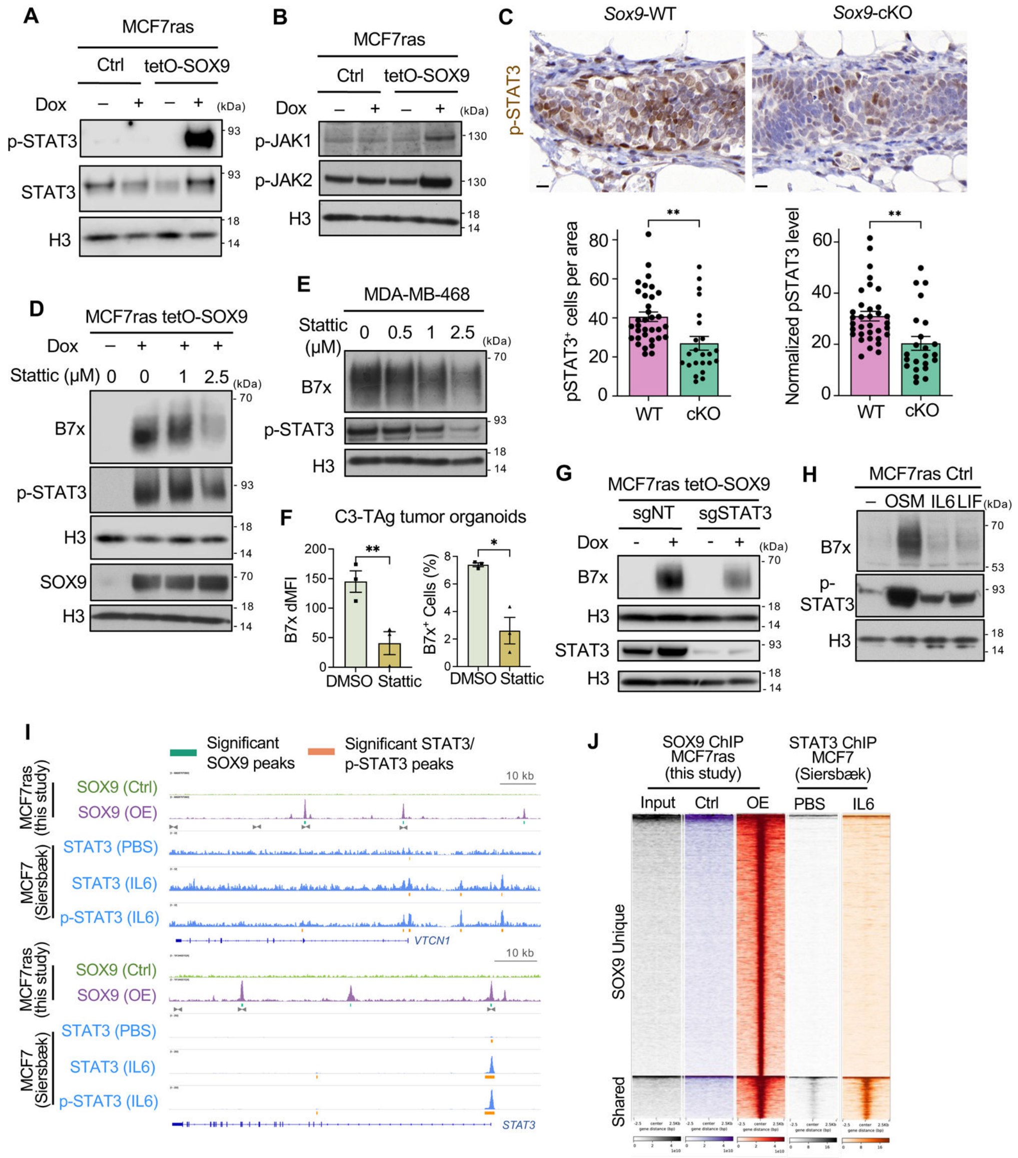

Figure 5. SOX9 upregulates B7x through activating the STAT3 pathway and direct binding to the B7x locus.

(A) Western blot of STAT3 and p-STAT3 in MCF7ras Ctrl and tetO-SOX9 cells.

(B) Western blot of p-JAK1 and p-JAK2 in MCF7ras Ctrl and tetO-SOX9 cells.

(C) Representative images of p-STAT3 IHC in MINs and quantification of p-STAT3$^+$ cell numbers per 10,000 μm^2 MIN area and pSTAT3 intensity in MINs. 34 MINs from 3 *Sox9*-WT mice and 23 MINs from 3 *Sox9*-cKO mice were analyzed. **p < 0.01 by unpaired Student's t-test. Scale bars, 10 μm.

(D) Western blot of B7x, p-STAT3 and SOX9 in MCF7ras tetO-SOX9 cells treated with the indicated concentrations of Stattic and doxycycline (dox) for 3 days.

(E) Western blot of B7x and p-STAT3 in MDA-MB-468 cells treated with the indicated concentrations of Stattic for 3 days.

(F) B7x flow cytometry of C3-TAg tumor organoids treated with 1 μM Stattic or DMSO control for 3 days. B7x dMFI and positive cell percentages normalized to isotype ctrl were shown (mean of three independent experiments). $**p < 0.01$ and $*p < 0.05$ by paired Student's t-tests.

(G) Western blot of B7x and STAT3 in MCF7ras tetO-SOX9 sgNT or sgSTAT3 cells treated with dox for 3 days.

(H) Western blot of B7x and p-STAT3 in MCF7ras Ctrl cells treated with 50 ng/ml OSM, IL6 or LIF for 2 days.

(I) SOX9 ChIP-seq in MCF7ras Ctrl cells or SOX9-OE cells (this study) and published STAT3/p-STAT3 ChIP-seq in MCF7 cells (Siersbæk study) [48] at the *VTCN1* and *STAT3* loci. Grey triangles indicate primers for ChIP-qPCR (Figure S6E and S6F).

(J) Heatmaps showing the ChIP-seq signals at SOX9 binding sites (+/− 2.5 kb from the peak centers) separated by their overlap with STAT3 peaks published in the Sierbaek study [48].

See also Figures S6.

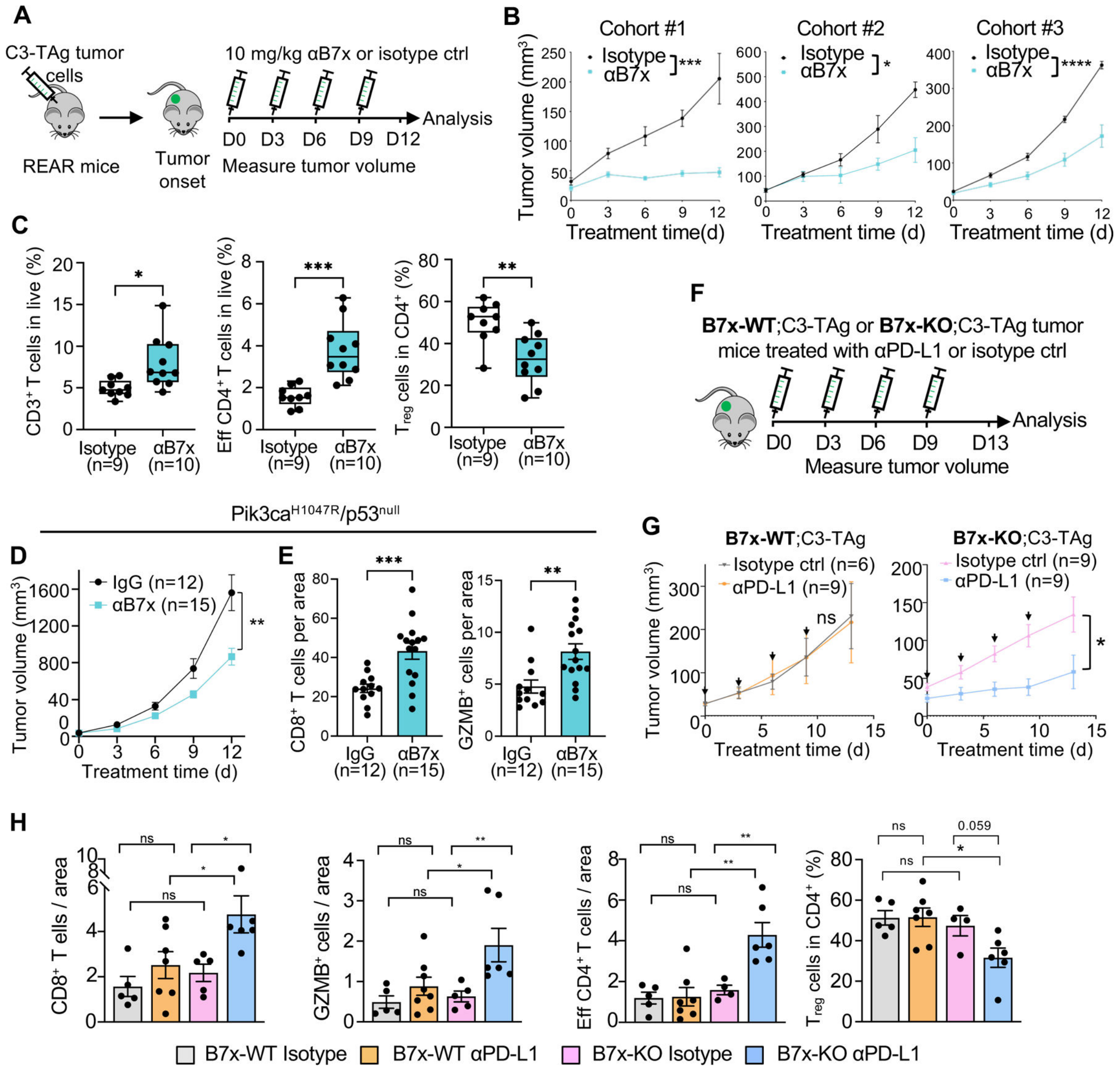

Figure 6. Targeting the SOX9-B7x axis activates anti-tumor immunity and confers response to anti-PD-L1 treatment.

(A) Schematic of αB7x treatment experiments.

(B) Tumor growth of C3-TAg allograft tumors treated with αB7x or isotype ctrl. Each cohort was allografts from an independent C3-TAg spontaneous tumor (αB7x: Cohort #1 n = 5, Cohort #2 n= 3, Cohort #3 n=8; Isotype ctrl: Cohort #1 n= 4, Cohort #2 n = 4, Cohort #3 n =9). Two-way ANOVA was used to determine statistical significance.

(C) Percentage of $CD3^+$ T cells and $CD4^+FOXP3^-$ effector T cells in total live cells, and $CD4^+FOXP3^+$ T_{reg} cells in $CD4^+$ T cells in tumors treated in (B). An unpaired Student’s t-test was used to determine statistical significance.

(D) Tumor growth curve of *Pik3ca*^{H1047R}/*p53*^{null} tumors treated with αB7x or isotype ctrl. Each data point represents the mean of one tumor. Two-way ANOVA was used to determine statistical significance.

(E) Numbers of $CD8^+$ T cells and $GZMB^+$ cells per 100,000 μm^2 tumor area, as treated in (H). Unpaired Student’s t-tests were used to determine statistical significance.

(F) Schematic of αPD-L1 treatment experiments in B7x-WT or B7x-KO;C3-TAg mice.
(G) Tumor growth curves of B7x-WT;C3-TAg or B7x-KO;C3-TAg mice treated with αPD-L1 or isotype ctrl (arrows indicate treatments). Two-way ANOVA was used to determine statistical significance.
(H) Numbers of CD8$^+$ T cells, GZMB$^+$ cells, and effector CD4$^+$ T cells per 100,000 μm^2 tumor area or percentage of Foxp3$^+$ T$_{reg}$ cells in CD4$^+$ cells in tumors as treated in (G). Each dot represents one tumor. Unpaired t-test was used to determine statistical significance. Data are summarized as mean ± SEM. ****$p < 0.0001$; ***$p < 0.001$; **$p < 0.01$; *$p < 0.05$; n.s., not significant. See also Figure S7.

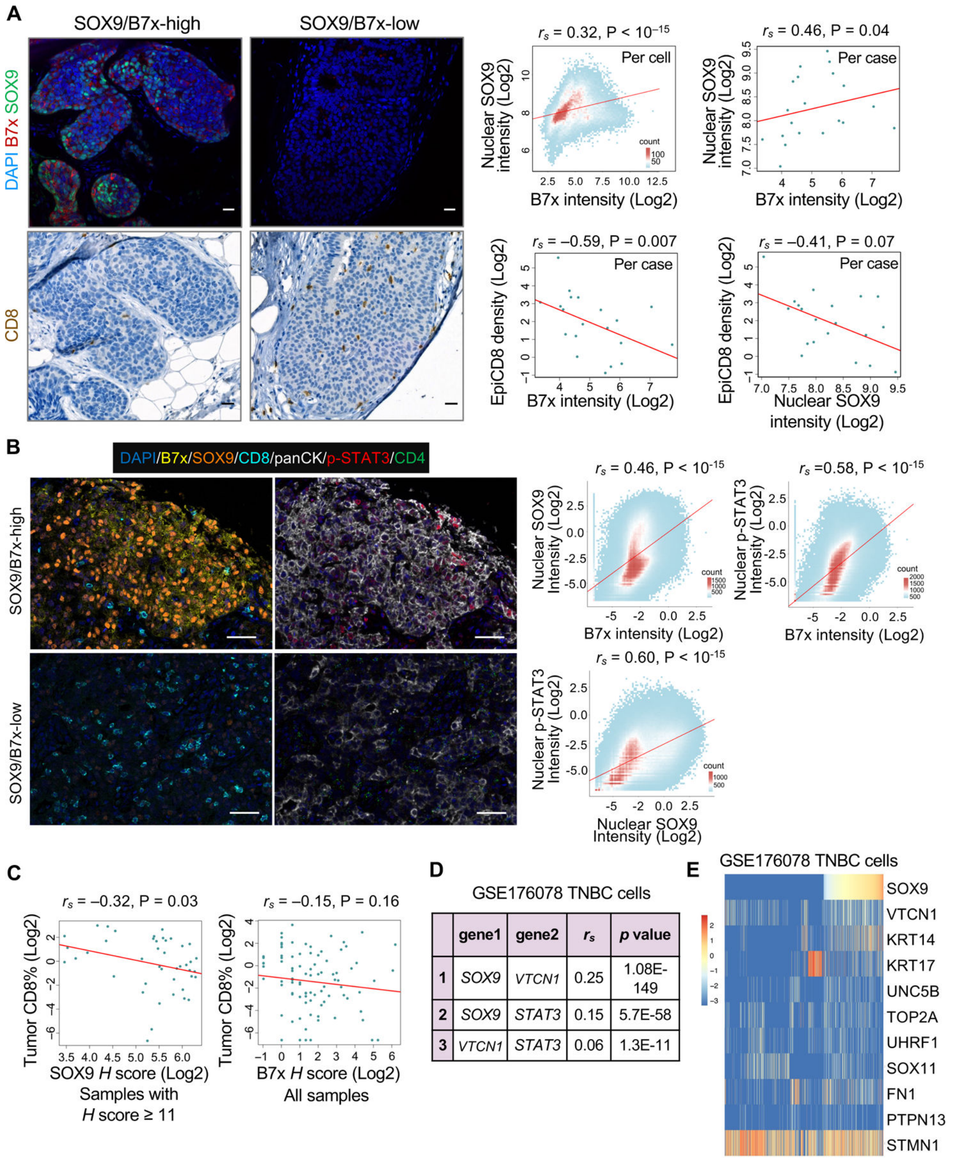

GSE176078 TNBC cells

	gene1	gene2	r_s	*p* value
1	*SOX9*	*VTCN1*	0.25	1.08E-149
2	*SOX9*	*STAT3*	0.15	5.7E-58
3	*VTCN1*	*STAT3*	0.06	1.3E-11

Figure 7. The correlation between the SOX9-B7x axis and reduced infiltrating T cells in human breast cancer samples.

(A) Representative images of SOX9, B7x, and CD8 immunostaining in 20 cases of human breast DCIS, and correlation analyses between these markers (Log_2(intensity)) among single DCIS cells or DCIS cases. Spearman's correlation coefficient was calculated. Scale bars, 20 µm.

(B) Representative images of SOX9, B7x, p-STAT3, pan-CK, CD8 and CD4 multiplex imaging in a tissue microarray (TMA) of 95 cases of human breast cancer, and correlation analyses between SOX9, p-STAT3 and B7x expression (Log_2(intensity+0.01)) at the single cell level. Spearman's correlation coefficient was calculated. Scale bars, 50 µm.

(C) Correlation analyses between tumor $CD8^+$ cell frequencies and SOX9 or B7x *H* score (Log_2(frequencies or *H* score+0.01)) among cancer cases in the TMA. Spearman's correlation coefficient was calculated.

(D) Spearman's correlation coefficient between indicated genes in published human TNBC single-cell RNA-seq dataset [52].

(E) Heatmap showing the expression of basal-cell and EMP genes at the single-cell level (color scale, Log_2(expression+0.1)). Samples were ranked based on *SOX9* expression.

See also Figure S8.

Key resources table

REAGENT or RESOURCE	SOURCE	IDENTIFIER
Antibodies		
Rabbit anti-CD3 (SP7)	Fisher Scientific	Cat#RM9107S0; RRID:AB_149923
Rabbit anti-CD4 (D7D2Z)	Cell Signaling Technology	Cat#25229S; RRID:AB_2798898
Rabbit anti-human CD8 (D8A8Y)	Cell Signaling Technology	Cat#85336S; RRID:AB_2800052
Rabbit anti-mouse CD8 (D4W2Z)	Cell Signaling Technology	Cat#98941S; RRID:AB_2756376
Rabbit anti-mouse Granzyme B (E5V2L)	Cell Signaling Technology	Cat#44153S; RRID:AB_2857976
Rabbit anti-mouse perforin (E3W4I)	Cell Signaling Technology	Cat#31647; RRID: AB_2857978
Rat anti-FOXP3 (FJK-16s)	eBioscience	Cat#14-5773-82; RRID:AB_467576
Rabbit anti-SOX9 (D8G8H)	Cell Signaling Technology	Cat#82630S; RRID:AB_2665492
Rabbit anti-B7x (D1M8I)	Cell Signaling Technology	Cat#14572S; RRID:AB_2750878
Anti-PD-L1 (MIH5)	eBioscience	Cat#14-5982-82; RRID:AB_467781
anti-Keratin 8	Developmental Studies Hybridoma Bank	Cat#AB_531826; RRID:AB_531826
Rabbit anti-Keratin 14	BioLegend	Cat#905304; RRID:AB_2616896
Chicken anti-Keratin 14	BioLegend	Cat#906004; RRID:AB_2616962
Goat anti-rabbit IgG AF647	Jackson ImmunoResearch	Cat#111-605-144; RRID:AB_2338078
Goat anti-rat IgG AF568	Invitrogen	Cat#A-11077; RRID:AB_2534121
Goat anti-mouse IgG AF568	Invitrogen	Cat#A-11031; RRID:AB_144696
Donkey anti-goat AF568	Invitrogen	Cat#A-11057; RRID:AB_142581
Goat anti-chicken IgY AF488	Jackson ImmunoResearch	Cat#103-545-155; RRID:AB_2337390
ImmPRESS HRP goat anti-rabbit IgG Polymer Reagent	Vector Laboratories	Cat#MP-7401; RRID:AB_2336529
ImmPRESS HRP goat anti-rat IgG Polymer Reagent	Vector Laboratories	Cat#MP-7404; RRID:AB_2336531
anti-SOX9-AF488 (EPR14335)	Abcam	Cat#ab196450; RRID:AB_2665383
anti-B7x-AF647 (EPR20236)	Abcam	Cat#ab225488
anti-E-Cadherin (36/E-CADHERIN)	BD Biosciences	Cat#BDB610182; RRID:AB_397581
anti-CD4 (4D12)	Leica Biosystems	Cat#PA0427
Rabbit anti-p-STAT3 (D3A7)	Cell Signaling Technology	Cat#9145S; RRID:AB_2491009
Rabbit anti-SOX9	Millipore	Cat#AB5535; RRID:AB_2239761
anti-CD8	Dako	Cat#M7103; RRID:AB_2075537
anti-pan-CK	Dako	Cat#M3515; RRID:AB_2132885
Mouse anti-STAT3 (124H6)	Cell Signaling Technology	Cat#9139S; RRID:AB_331757
Rabbit anti-p-JAK1	Cell Signaling Technology	Cat#3331S; RRID:AB_2265057
Rabbit anti-p-JAK2 (C80C3)	Cell Signaling Technology	Cat#3776S; RRID:AB_2617123
anti-β-actin	BD Biosciences	Cat#612656;RRID:AB_2289199
Mouse anti-Histone H3 (1B1B2)	Cell Signaling Technology	Cat#14269S; RRID:AB_2756816
anti-mouse B7x-APC (HMH4-5G1)	BioLegend	Cat#139407; RRID:AB_2565217
anti-mouse B7x-PE (HMH4-5G1)	BioLegend	Cat#139405; RRID:AB_10613286

REAGENT or RESOURCE	SOURCE	IDENTIFIER
anti-human B7x-APC (MIH43)	BioLegend	Cat#358107; RRID:AB_2562580
anti-human B7x-PE (MIH43)	BioLegend	Cat#358103; RRID:AB_2562080
anti-human CD3-APC (SK7)	BioLegend	Cat#981012; RRID:AB_2876776
anti-human HLA-A2-APC (BB7.2)	BioLegend	Cat#343307; RRID:AB_2561566
anti-mouse CD45-Pacific Blue (30-F11)	BioLegend	Cat#103125; RRID:AB_493536
anti-mouse CD45-FITC (30-F11)	BioLegend	Cat#103107; RRID:AB_312972
anti-mouse CD3-APC (17A2)	BioLegend	Cat#100235; RRID:AB_2561455
anti-mouse CD3-FITC (17A2)	BioLegend	Cat#100203; RRID:AB_312660
anti-mouse CD3-PE (17A2)	BioLegend	Cat#100205; RRID:AB_312662
anti-mouse CD3-BV750 (17A2)	BioLegend	Cat#100249; RRID:AB_2734148
anti-mouse CD4-APC/Cy7 (GK1.5)	BioLegend	Cat#100413; RRID:AB_312698
anti-mouse CD4-BUV496 (GK1.5)	BD Biosciences	Cat#612952; RRID:AB_2813886
anti-mouse CD8a-PE (53-6.7)	BioLegend	Cat#100707; RRID:AB_312746
anti-mouse CD8a-PE/Dazzle594 (53-6.7)	BioLegend	Cat#100761; RRID:AB_2564026
anti-mouse CD8a-BV711 (53-6.7)	BioLegend	Cat#100747; RRID:AB_11219594
anti-mouse B7-H3-PE (MIH35)	BioLegend	Cat#135605; RRID:AB_2073573
anti-mouse PD-L1-PE (10F.9G2)	BioLegend	Cat#124307; RRID:AB_2073557
anti-mouse Ter119-biotin (TER-119)	BioLegend	Cat#116203; RRID:AB_313704
anti-mouse CD31-biotin (390)	BioLegend	Cat#102404; RRID:AB_312899
anti-mouse CD45-biotin (30-F11)	BioLegend	Cat#103103; RRID:AB_312968
Streptavidin-V450	BD Biosciences	Cat#560797; RRID:AB_2033992
Streptavidin-BUV395	BD Biosciences	Cat#564176; RRID:AB_2869553
anti-EpCam-APC (G8.8)	BioLegend	Cat#118213; RRID:AB_1134105
anti-EpCam-PerCP/Cy5.5 (G8.8)	BioLegend	Cat#118219; RRID:AB_2098647
anti-CD49f-PerCP/Cy5.5 (GoH3)	BD Biosciences	Cat#562475; RRID:AB_11151910
anti-CD166-PE (eBioALC48)	eBioscience	Cat#12-1661-82; RRID:AB_823125
anti-CD117-PE/Cy7 (2B8)	BD Biosciences	Cat#561681; RRID:AB_10893022
anti-Sca1-APC/Cy7 (D7)	BioLegend	Cat#108125; RRID:AB_10639725
anti-CD49b-AF488 (HMα2)	BioLegend	Cat#103510; RRID:AB_492851
anti-CD25-PerCP/Cy5.5 (PC61)	BioLegend	Cat#102029; RRID:AB_893291
anti-CD11b-BV510 (M1/70)	BioLegend	Cat#101245; RRID:AB_2561390
anti-CD11b-PE/Dazzle594 (M1/70)	BioLegend	Cat#101255; RRID:AB_2563647
anti-Ly6C-PE/Dazzle594 (HK1.4)	BioLegend	Cat#128043; RRID:AB_2566576
anti-Ly6C-biotin (AL-21)	BD Biosciences	Cat#557359; RRID:AB_396663
anti-Ly6G-APC (1A8)	BioLegend	Cat#127613; RRID:AB_1877163
anti-Ly6G-PerCP-eFluor710 (1A8)	eBioscience	Cat#46-9668-82; RRID:AB_2573893
anti-CD11c-FITC (N418)	BioLegend	Cat#117305; RRID:AB_313774
anti-CD11c-BUV496 (N418)	BD Biosciences	Cat#750450; RRID:AB_2874611
anti-F4/80-PE/Cy5 (BM8)	BioLegend	Cat#123111; RRID:AB_893494

REAGENT or RESOURCE	SOURCE	IDENTIFIER
anti-F4/80-eFluor 506 (BM8)	eBioscience	Cat#69-4801-82; RRID:AB_2637190
anti-FOXP3-PE/Cy5 (FJK-16s)	eBioscience	Cat#35-5773-82; RRID:AB_11218094
Anti-Rat and Anti-Hamster Ig κ /Negative Control Compensation Particles Set	BD Biosciences	Cat#552845; RRID:AB_10058522
Anti-Mouse Ig, κ/Negative Control Compensation Particles Set	BD Biosciences	Cat#552843; RRID:AB_10051478
anti-NK1.1-BV785 (PK136)	BioLegend	Cat#108749; RRID:AB_2564304
anti-CD169-eFluor660 (SER-4)	BioLegend	Cat#50-5755-82; RRID:AB_2574241
anti-CD4-Alexa Fluro 700 (RM4-5)	BioLegend	Cat#100536; RRID:AB_493701
anti-CD19-APC/Cy7 (6D5)	BioLegend	Cat#115529; RRID:AB_830706
anti-CD115-PE/Cy7 (AFS98)	BioLegend	Cat#135523; RRID:AB_2566459
anti-hB7x (H19)	This paper	N/A
anti-mB7x (1H3)	Jeon et al. 50	N/A
InVivoPlus anti-mouse CD4	Bio X Cell	Cat#BP0003-1
InVivoMAb anti-mouse CD8β (Lyt 3.2)	Bio X Cell	Cat#BE0223; RRID:AB_2687706
InVivoPlus rat IgG2b isotype control, anti-keyhole limpet hemocyanin	Bio X Cell	Cat#BP0090
InVivoMAb rat IgG1 isotype control, anti-horseradish peroxidase	Bio X Cell	Cat#BE0088; RRID:AB_1107775
InVivoMAb mouse IgG1 isotype control	Bio X Cell	Cat#BE0083; RRID:AB_1107784
InVivoMAb anti-mouse PD-L1 (B7-H1)	Bio X Cell	Cat#BE0101; RRID:AB_10949073
InVivoMAb rat IgG2b isotype control, anti-keyhole limpet hemocyanin	Bio X Cell	Cat#BE0090; RRID:AB_1107780
Rabbit (DA1E) mAb IgG XP® Isotype Control	Cell Signaling Technology	Cat#3900S; RRID:AB_1550038
Bacterial and virus strains		
NEB® Stable Competent E. coli (High Efficiency)	New England Biolabs	Cat#C3040I
Biological samples		
Human tissue microarray of breast carcinoma (BR1902)	US Biomax	https://www.tissuearray.com/tissue-arrays/Breast/BR1902
Human DCIS FFPE sections	Montefiore Einstein Cancer Center	N/A
Human PBMCs from healthy donors	New York Blood Center	N/A
Chemicals, peptides, and recombinant proteins		
DAPI	Biotium	Cat#40009
Ghost Dye Red 780	Tonbo	Cat#13-0865-T100
Dulbecco’s Modified Eagle Medium (DMEM)	Corning	Cat#10-017-CV
Fetal Bovine Serum (FBS)	VWR	Cat#97068-085
RPMI1640	Gibco	Cat#11875085
Doxycycline	Sigma-Aldrich	Cat#D9891
Stattic	Cayman Chemical Company	Cat#14590
Recombinant Human Oncostatin M (OSM) Protein	R&D Systems	Cat#295-OM-010cf
Recombinant Human LIF (carrier-free)	BioLegend	Cat#593902

REAGENT or RESOURCE	**SOURCE**	**IDENTIFIER**
Recombinant Human IL-6 (carrier-free)	BioLegend	Cat#570802
Ruxolitinib	Cayman Chemical Company	Cat#11609
Advanced DMEM/F12 medium	Life Technology	Cat#12634010
hEGF	Sigma-Aldrich	Cat#E9644
FGF2	EMD Millipore	Cat#GF003
Heparin	Sigma-Aldrich	Cat#H4784
Y-27632	Cayman Chemical Company	Cat#10005583-10
Matrigel	Corning	Cat#354234
2-hydroxyethyl methacrylate (Poly-HEMA)	Sigma-Aldrich	Cat#P3932-25G
PBS	Fisher Scientific	Cat#SH3025601
0.05% Trypsin-EDTA	Fisher Scientific	Cat#MT25052CI
Puromycin	Fisher Scientific	Cat#54-022-225MG
Blasticidin	Cayman Chemical Company	Cat#14499-50
30% hydrogen peroxide	Sigma-Aldrich	Cat#31642
antigen unmasking solution	Vector Laboratories	Cat#H-3300
Thermo Scientific™ Halt™ Protease Inhibitor Cocktails	Fisher Scientific	Cat#PI87786
Thermo Scientific™ Halt™ Phosphatase Inhibitor	Fisher Scientific	Cat#PI-78420
4-12% NuPAGE Bis-Tris Protein Gels	Invitrogen	Cat#NP0322BOX
PVDF membrane	Millipore	Cat#IPVH00010
Western Lightning ECL Pro	PerkinElmer	Cat#NEL121001EA
DMEM/F12 medium	Corning	Cat#10-092-CV
Collagenase 3	Worthington	Cat#LS004182
DNase I	Worthington	Cat#LS002139
hyaluronidase	Worthington	Cat#LS002592
RBC lysis buffer	eBioscience	Cat#00-4300-54
Dispase	Worthington	Cat#LS02109
0.5M EDTA	Fisher Scientific	Cat#PRV4231
eBioscience Transcription Factor Staining Buffer	Thermo Fisher	Cat#00-5523-00
NCTC-109 medium	Thermo Fisher	Cat#21340039
Non-essential amino acids (NEAA)	Invitrogen	Cat#11140-050
penicillin and streptomycin	Corning	Cat#30-002-CI
CTS OpTmizer media	Gibco	Cat#A1048501
L-glutamine	Sigma-Aldrich	Cat#G7513-100ML
anti-CD3/CD28 Dynabeads	Gibco	Cat#11161D
Recombinant Human IL-2 (carrier-free)	BioLegend	Cat#589102
retronectin	Takara	Cat#T100A
sodium pyruvate	Invitrogen	Cat#11360-070
β-mercaptoethanol	Sigma-Aldrich	Cat#M6250-100ML
mitomycin-c	Sigma-Aldrich	Cat#M7949-2MG

REAGENT or RESOURCE	**SOURCE**	**IDENTIFIER**
CellTrace Violet (CTV)	Invitrogen	Cat#C34571
HEPES	Sigma-Aldrich	Cat#H3375-250G
Ruxolitinib (in vivo)	MedChem Express	Cat#HY-50856
CMC-Na	Selleck Chemicals	Cat#S6703
32% Paraformaldehyde (Formaldehyde)	Electron Microscopy Sciences	Cat#15714-S
Glycine	Sigma-Aldrich	Cat#G7126-10MG
Dynabeads Protein A	Invitrogen	Cat#0002D
phenol:chloroform:isoamyl alcohol	Sigma-Aldrich	Cat#77677-100ML
Critical commercial assays		
Human LIF ELISA Kit	Invitrogen	Cat#BMS242
SYBR Green PCR Master Mix	Applied Biosystems	Cat#A25778
Direct-zol RNA Miniprep Plus kit	Zymo Research	Cat#R2050S
DAB Peroxidase (HRP) Substrate Kit	Vector Laboratories	Cat#SK-4100
7-Color Opal Polaris reagent kit	Akoya Biosciences	Cat#NEL871001KT
DC Protein Assay kit	Bio-Rad	Cat#500-0116
High-Capacity cDNA Reverse Transcription Kit	Applied Biosystems	Cat#4368814
Protein G resin columns	GenScript	Cat#L00681
Lymphoprep	Stemcell Technologies	Cat#07851
iMag human $CD4^+$ or $CD8^+$ lymphocyte enrichment sets	BD Biosciences	Cat#557941
Human CD4 magnetic beads	Miltenyi Biotec	Cat#130-045-101
Human CD8 magnetic beads	Miltenyi Biotec	Cat#130-045-201
10X Genomics Chromium Next GEM 3' v3.1 kit	10X Genomics	Cat#1000269
Deposited data		
Raw and processed data for RNA-seq, ChIP-seq, and scRNA-seq	This paper	GEO: GSE219110
Published microarray data (*Sox9*-WT/cKO ER^- luminal cells; *Sox9*-GFP^{low} and *Sox9*-GFP^{high} luminal cells)	Christin et al. [19]	GEO: GSE135892
Published ChIP-seq data (MCF7)	Siersbæk et al. [48]	GEO: GSE126004
Published scRNA-seq data (TNBC)	Wu et al. [52]	GEO: GSE176078
Public TCGA BRCA dataset	The Cancer Genomics Atlas	https://xena.ucsc.edu
Experimental models: Cell lines		
Human: HEK293T	ATCC	Cat#CRL-3216; RRID:CVCL_0063
Human: MCF7ras Ctrl and tetO-SOX9	Guo et al. [27]	N/A
Human: MDA-MB-468	ATCC	Cat#HTB-132; RRID:CVCL_0419
Human: SK-BR3	ATCC	Cat#HTB-30; RRID:CVCL_0033
Human: HCC1937	ATCC	Cat#CRL-2336; RRID:CVCL_0290
Mouse: 4T1	ATCC	Cat#CRL-2539; RRID: CVCL_0125
NS0 myeloma cells	Sigma-Aldrich	Cat#85110503-1VL
Mouse: 3T3	ATCC	Cat#CRL-1658; RRID:CVCL_0594

REAGENT or RESOURCE	SOURCE	IDENTIFIER
Mouse organoid: $\mathit{Pik3ca}^{H1047R}/\mathit{p53}^{nul}$	Boutet et al. [40]	N/A
Mouse organoid: *Sox9*$^{\mathrm{Fl/Fl}}$;C3-TAg tumor organoid	This paper	N/A
Mouse organoid: *Sox9*-GFP;C3-TAg mammary epithelial organoid	This paper	N/A
Mouse organoid: *Sox9*-cKO;C3-TAg mammary epithelial organoid	This paper	N/A
Mouse organoid: BALB/c mammary epithelial organoid	This paper	N/A
Mouse organoid: B7x$^{-/-}$ mammary epithelial organoid	This paper	N/A
Experimental models: Organisms/strains		
Mouse: FVB-Tg(C3-1-TAg)cJeg/JegJ	The Jackson Laboratory	JAX:013591; RRID:IMSR_JAX:013591
Mouse: B6.129S7-Sox9tm2Crm/J	The Jackson Laboratory	JAX:013106; RRID:IMSR_JAX:013106
Mouse: FVB/N-Tg(C3-1-TAg)cJeg/2JegJ	The Jackson Laboratory	JAX:030386; RRID:IMSR_JAX: 030386
Mouse: B6.129S7-Rag1tm1Mom/J	The Jackson Laboratory	JAX:002216; RRID:IMSR_JAX: 002216
Mouse: FVB-Tg(MMTV-iCre/CAG-CAC-ECFP)	Christin et al. [18]	N/A
Mouse: STOCK Tg(Sox9-EGFP)EB209Gsat/Mmucd	Christin et al. [18]	N/A
Mouse: B7x$^{-/-}$ (BALB/c background)	Jeon et al. [50]	N/A
Oligonucleotides		
qRT-PCR and ChIP-qPCR primers	This paper	Table S1
shSOX9 hairpins	Guo et al. [27]	N/A
sgSTAT3 (GTCAGGATAGAGATAGACCAG)	This paper	N/A
sgNT (GCGAGGTATTCGGCTCCGCG)	This paper	N/A
Recombinant DNA		
pLVX-puro	Christin et al. [18]	N/A
pLVX-SOX9	Christin et al. [18]	N/A
tetO-SOX9	Guo et al. [27]	N/A
pLKO.1-puro	Takara	Cat#632164
LentiCRISPRv2-blast	Addgene	Cat#83480; RRID:Addgene_83480
NYESO alpha/beta into TRBC1 HDRT Source (pTR 262)	Addgene	Cat#112022; RRID:Addgene_112022
NYESO beta/alpha into TRAC HDRT Source (pTR 169)	Addgene	Cat#112021; RRID:Addgene_112021
pCDH-EF1-IRES-EGFP	Addgene	Cat#128059; RRID:Addgene_128059
pCDH-EF1-TCRα/β-IRES-EGFP	This paper	N/A
pHIV-dTomato	Addgene	Cat#21374; RRID:Addgene_21374
pHIV-mB7x-dTomato	This paper	N/A
Software and algorithms		
GraphPad Prism (version 9.3.0)	Dotmatics	https://www.graphpad.com
FlowJo (version 10.8.0)	BD Biosciences	https://www.flowjo.com
R (version 4.2.2)	The R Foundation	https://www.r-project.org/
ImageJ (FIJI, version 2.9.0)	Schindelin et al. [72]	https://imagej.net/software/fiji/

REAGENT or RESOURCE	**SOURCE**	**IDENTIFIER**
QuPath (version 0.3.2)	Bankhead et al. [73]	https://qupath.github.io
SlideBook 6.0	Intelligent Imaging Innovations	https://www.intelligent-imaging.com/slidebook
CaseViewer (version 2.4)	3DHISTECH	https://www.3dhistech.com/solutions/caseviewer/
Phenochart (version 1.1.0)	Akoya Biosciences	https://www.akoyabio.com/support/software/phenochart-whole-slide-viewer/
inForm (version 2.6.0)	Akoya Biosciences	https://www.akoyabio.com/phenoimager/software/inform-tissue-finder/
ggplot2 (version 3.4.0)	N/A	https://ggplot2.tidyverse.org/
Phenoptr (version 0.3.2)	Akoya Biosciences	https://akoyabio.github.io/phenoptr/
phenoptrReports (version 0.3.3)	Akoya Biosciences	https://akoyabio.github.io/phenoptrReports/
STAR (version 2.4.0)	N/A	https://github.com/alexdobin/STAR
pHeatmap (version 1.0.12)	N/A	https://www.rdocumentation.org/packages/pheatmap/versions/1.0.12/topics/pheatmap
scran (version 1.26.0)	Lun et al. [79]	https://bioconductor.org/packages/release/bioc/html/scran.html
Seurat (version 3.2.2 and 4.1.1)	Stuart et al. [78]	https://satijalab.org/seurat/
Cell Ranger (version 3.1.0)	10X Genomics	https://support.10xgenomics.com/single-cell-multiome-atac-gex/software/downloads/latest?
DESeq2 (version 1.28.1 and 1.30.1)	Love et al. [77]	https://bioconductor.org/packages/release/bioc/html/DESeq2.html
IGV (version 2.8.6)	Broad Institute	https://software.broadinstitute.org/software/igv/download
IPA	Qiagen	https://analysis.ingenuity.com/pa/installer/select
GSEA (version 4.2.2)	Broad Institute	http://www.broadinstitute.org/gsea
bowtie2 (version 2.4.2)	N/A	https://bowtie-bio.sourceforge.net/bowtie2/index.shtml
BBTools seal.sh (version 38.90)	Joint Genome Institute	https://jgi.doe.gov/data-and-tools/bbtools/bb-tools-user-guide/seal-guide/
Genrich (version 0.6.1)	N/A	https://github.com/jsh58/Genrich
Deeptools (version 3.5.0)	N/A	https://deeptools.readthedocs.io/en/develop/content/installation.html
enrichR (version 3.0)	Kuleshov et al. [45]	https://maayanlab.cloud/Enrichr/
Homer (version 4.11)	UCSD	http://homer.ucsd.edu/homer/
BEDTools (version 2.30.0)	N/A	https://bedtools.readthedocs.io/en/latest/content/installation.html
fgsea (version 1.14.0)	Sergushichev et al. [80]	https://bioconductor.org/packages/release/bioc/html/fgsea.html
TIMER 2.0	Li et al. [53]	http://timer.cistrome.org/
BioRender	BioRender	https://app.biorender.com/
Other		